applied sciences

MDPI

Article

Analysis of Photocatalytic Properties of Poly(Methyl Methacrylate) Composites with Titanium(IV) and Ruthenium(III) Complexes

Barbara Kubiak [1,*], Adrian Topolski [1], Aleksandra Radtke [1,*], Tadeusz Muzioł [1], Olga Impert [1], Anna Katafias [1], Rudi van Eldik [1,2] and Piotr Piszczek [1]

[1] Department of Inorganic and Coordination Chemistry, Faculty of Chemistry, Nicolaus Copernicus University in Toruń, Gagarina 7, 87-100 Toruń, Poland; topolski@umk.pl (A.T.); tadeuszmuziol@wp.pl (T.M.); oimpert@umk.pl (O.I.); katafias@umk.pl (A.K.); rudi.vaneldik@fau.de (R.v.E.); piszczek@umk.pl (P.P.)

[2] Department of Chemistry and Pharmacy, University of Erlangen-Nuremberg, Egerlandstrasse 1, 91058 Erlangen, Germany

* Correspondence: basiak0809@gmail.com (B.K.); aradtke@umk.pl (A.R.)

Abstract: This study explores poly(methyl methacrylate) (PMMA)-based composites as potential alternatives to conventional TiO_2-based photocatalysts. Specifically, it examines PMMA composites enriched with oxo–titanium(IV) complexes, $[Ti_8O_2(O^iPr)_{20}(man)_4]$ (**1**), $[Ti_4O(O^iPr)_{10}(O_3C_{14}H_8)_2]$ (**2**), and $[Ti_6O_4(O^iPr)_2(O_3C_{14}H_8)_4(O_2CEt)_6]$ (**3**), alongside ruthenium(III) complexes, $K[Ru(Hedta)Cl]\cdot 2H_2O$ (**4**) and $[Ru(pic)_3]\cdot H_2O$ (**5**). We assessed the physicochemical, adsorption, and photocatalytic properties of these composites with structural analyses (Raman spectroscopy, X-ray absorption (XAS), and SEM-EDX), confirming the stability of complexes within the PMMA matrix. Composites containing titanium(IV) compounds demonstrated notably higher photocatalytic efficiency than those with ruthenium(III) complexes. Based on activity profiles, composites were categorized into three types: (i) UV-light active (complexes (**1**) and (**2**)), (ii) visible-light active (complexes (**4**) and (**5**)), and (iii) dual-range active (complex (**3**)). The results highlight the strong potential of titanium(IV)–PMMA composites for UV-driven photocatalysis. Moreover, their activity can be extended to the visible range after structural modifications. Ruthenium(III)–PMMA composites, in turn, showed superior performance under visible light. Overall, PMMA composites with titanium(IV) or ruthenium(III) complexes demonstrate promising photocatalytic properties for applications using both UV and visible light ranges.

Keywords: titanium(IV)–oxo complexes; ruthenium(III) complexes; PMMA-based composites; photocatalytic activity; adsorptive properties; physicochemical properties

Academic Editor: Antonio Miotello

Received: 16 January 2025
Revised: 31 January 2025
Accepted: 3 February 2025
Published: 7 February 2025

Citation: Kubiak, B.; Topolski, A.; Radtke, A.; Muzioł, T.; Impert, O.; Katafias, A.; van Eldik, R.; Piszczek, P. Analysis of Photocatalytic Properties of Poly(Methyl Methacrylate) Composites with Titanium(IV) and Ruthenium(III) Complexes. *Appl. Sci.* **2025**, *15*, 1679. https://doi.org/10.3390/app15041679

1. Introduction

Rapid industrial growth has increased the need for more efficient methods to address water and air pollution [1–4]. Organic dyes, such as methylene blue and rhodamine B, pose significant health risks due to their toxic effects, including skin and respiratory irritation [5,6]. Traditional methods, like adsorption and filtration, are effective, but they come with limited capacity and high energy requirements, diminishing their efficiency [7,8]. Photocatalysis offers significant advantages, particularly in environmental applications. It effectively degrades organic pollutants, neutralizes harmful substances, and eliminates microorganisms, making it a key water and air purification method [9–11]. Among photocatalysts, titanium dioxide (TiO_2) is the most widely used due to its stability and effectiveness [12–14]. However, its practical application is constrained by its ability to absorb

light mainly in the UV range, which constitutes just 5% of sunlight [15–17]. To overcome this limitation, current research focuses on modifying TiO_2 or the creation of TiO_2-based materials capable of absorbing visible light, thereby enhancing their efficiency and applicability [18–20].

Titanium–oxo complexes (TOCs) are an important research direction for modifying TiO_2-based materials. These compounds are characterized by stable structures in which the $\{Ti_aO_b\}$ core can be stabilized by various organic ligands, e.g., alkoxide and carboxylate [21–26]. Coordination of appropriate ligands reduces the HOMO–LUMO gap, causing radiation absorption in a wider range. An example is the study by Pei et al., who investigated TOCs with $\{Ti_{10}O_{12}\}$ cores stabilized by benzoic acid derivatives. They exhibited that using 4-methoxybenzoate ligands significantly enhanced the photocatalytic efficiency of these complexes against rhodamine B [27]. This effect was attributed to a reduction in the gap from 3.34 eV to 2.47 eV. The proposed mechanism of photocatalytic activity was related to the ligand-to-metal charge transfer (LMCT), which facilitated the generation of reactive oxygen species (ROS) responsible for degrading the dyes into H_2O and CO_2 [28,29]. The structure of the $\{Ti_aO_b\}$ core can also influence the photocatalytic activity of TOCs. Results of our work on oxo complexes with core structures $\{Ti_6O_6\}$, $\{Ti_4O_2\}$, $\{Ti_3O\}$, and $\{Ti_6O_4\}$, stabilized by 9-fluorenecarboxylate ligands, confirm this effect. Systems containing $\{Ti_6O_4\}$ and $\{Ti_6O_6\}$ cores tended to shift the absorption maximum toward the UV range, whereas simpler units ($\{Ti_3O\}$ and $\{Ti_4O_2\}$) shifted it toward visible light [30]. Continuing this line of research, we replaced carboxylate ligands with α-hydroxy carboxylate ligands (i.e., with 9-OH-9-fluorenecarboxylate [31] and mandelate ligands [32]). Our aim was to stabilize the structures of oxo complexes using new ligands, synthesize complexes with novel core structures, and evaluate the impact of these factors on their photocatalytic activity.

While analyzing the possibilities of modifying TiO_2-based materials, we became interested in a method to enhance their photocatalytic activity through doping with ruthenium complexes [33–38]. In recent years, the electrocatalytic and photocatalytic activity of single Ru atoms was investigated [39]. However, ruthenium(II) tris(bipyridine) complexes are regarded as benchmark photocatalysts due to their strong light absorption and long excited-state lifetimes [40–42]. Relatively few reports address the photocatalytic activity of Ru(III) complexes, although they have gained attention in recent years [43–45]. This led us to investigate the effects of ruthenium(III) complexes on organic dye degradation and compare their performance with oxo–Ti(IV) complexes. The photocatalytic mechanism of Ru(III) complexes involves metal-to-ligand charge transfer (MLCT) upon light irradiation, generating an excited [RuIII]* complex, which can act as an oxidant or a reductant, depending on the presence of electron acceptors or donors [46].

Studies on ruthenium complexes conducted by Fleming et al. showed that incorporating them into a poly(methyl methacrylate) (PMMA) matrix to enhance the stability of the complex enabled electron transfer measurements based on MLCT [47]. Moreover, it reduced the tendency for grain aggregation, thereby improving the practical applicability of such systems. A similar challenge arises with titanium–oxo complexes (TOCs), which are commonly used in photocatalytic experiments in powder form. This form makes them prone to hydrolysis, significantly complicating their practical application. To overcome this limitation, the stability of TOCs can be enhanced by coordinating suitable ligands [48,49] or embedding them into a polymer matrix [30,50,51]. In our previous studies, we introduced oxo complexes into the PMMA matrix and evaluated the photocatalytic performance of the resulting composites, achieving promising results [30,42,50–52]. PMMA was chosen as the polymer matrix due to its transparency to visible light, excellent mechanical properties, and environmental stability. Furthermore, incorporating TiO_2 into the PMMA matrix has been shown to improve the thermal stability and electrical conductivity of the composites [53,54].

Despite these advantages, PMMA + TOC composites have not been widely investigated in photocatalytic applications, which provided additional motivation for our research. Incorporating the complex into a polymer matrix also addresses important environmental considerations. Hydrolysis products can contribute to additional contaminants that require removal, and their elevated concentrations, along with potential interactions with other substances, may present significant environmental risks.

2. Materials and Methods

2.1. Materials

Titanium–oxo complexes (**1**)–(**3**) were synthesized as reported in [31,32], while ruthenium complexes (**4**) and (**5**) were prepared following the procedures previously outlined [55,56]. Detailed information regarding the preparation of the studied compounds is provided in the Supplementary Information.

2.2. Analytical Procedures

The structures of the synthesized compounds (**1**)–(**5**) were characterized using IR spectrophotometry performed on a Perkin Elmer Spectrum 2000 FT-IR spectrometer (operating in the 400–4000 cm^{-1} range with KBr pellets) and Raman microscopy using a RamanMicro 200 spectrometer (PerkinElmer, Waltham, MA, USA). Raman spectra were recorded with a 785 nm laser (maximum power: 350 mW) across the 200–3200 cm^{-1} range, employing a 20× 0.40/FN22 objective lens and an exposure time of 15 s for each measurement. Solid-state 13C13C NMR spectra were obtained at 22 °C using a Bruker AMX 300 spectrometer (Cambridge Scientific Corp., Watertown, MA, USA). Elemental analyses were conducted with an Elementar vario Macro CHN analyzer (Elementar Analysensysteme GmbH, Hanau, Germany). Titanium content was determined as TiO_2, according to the method of Meth-Cohn et al. [57]. According to [58], ruthenium content was determined as RuO_2. Diffuse reflectance UV-Vis (UV-VIS-DRS) spectra, recorded between 200 and 800 nm on a Jasco V-750 spectrophotometer (JASCO Deutschland GmbH, Pfungstadt, Germany), were used to determine the absorption maxima.

2.3. Composite Film Preparation

The composite films were prepared through compound (**1**)–(**5**) dispersion (approximately 0.025, 0.062, 0.12, or 0.25 g in 5 mL of THF) into poly(methyl methacrylate) (PMMA). For this purpose, 1.0 g of PMMA was dissolved in 10 mL of THF, and the powdered samples of the complexes were added to the resulting solution to achieve concentrations of 2%, 5%, 10%, and 20%, respectively. After mixing for 120 min in an ultrasonic bath, the solution containing the dispersed complex powders was poured into a glass Petri dish and left at room temperature (in a glove box) to allow the solvent to evaporate slowly. The composite films, with a thickness of approximately 50 μm, were characterized using Raman spectroscopy. The complexes' size and dispersion pattern in the composite samples were analyzed using a Quanta scanning electron microscope with field emission (SEM, Quanta 3D FEG, Houston, TX, USA). X-ray absorption spectra were recorded at the National Synchrotron Radiation Centre SOLARIS on the PIRX beamline with a bending magnet, focusing on the Ti $L_{2,3}$-edge (440–510 eV). Finely ground powder samples were mounted on double-sided adhesive conductive graphite tape, while composite materials were similarly secured. Measurements for both sample types were conducted with a step size of 0.2 eV in the pre-edge region, 0.1 eV in the edge regions, and 0.5 eV in the high-energy range. Data acquisition was performed at room temperature under ultra-high vacuum (UHV) conditions, using total electron yield (TEY) and fluorescence yield (FY) detection modes. Each measurement was

repeated at least three times. The collected data were processed and deconvoluted using ATHENA software (v3) from the Demeter package [53].

2.4. Estimation of the Adsorption Capacity

The adsorption capacity of PMMA + TOCs films (TOCs = (**1**)–(**5**)) was determined by measuring changes in the absorbance of the dye solution (methylene blue (MB), rhodamine B (RhB) and crystal violet (CV)) (C = 1.0×10^{-5} M). The composites (26 × 26 mm) and 30 mL of the dye solution were placed in a laboratory bottle in a dark place. Spectra were recorded (JASCO Deutschland GmbH, Pfungstadt, Germany) in the range of 400–700 nm at 0, 1, 3, 5, 9, and 24 h by taking 3.5 mL of the solution into a quartz cuvette. The absorption maxima were recorded at 664, 590, and 554 nm for MB, RhB, and CV, respectively. The percentage of MB decolorization was calculated using the following equation:

$$\% \text{ dye decolourization} = \frac{(C_0 - C_t)}{C_0} \cdot 100\% \quad (1)$$

where C_0 is an initial dye concentration and C_t is a dye concentration at a given time t [54].

2.5. Estimation of the Photocatalytic Activity

The photocatalytic activity of PMMA + TOCs foils (TOCs = (**1**)–(**5**)) was estimated by monitoring the concentration changes of methylene blue (MB) and crystal violet (CV) in aqueous solution. Sample preparation included irradiating the samples with UVA or Vis radiation for 28 h and placing them in quartz cuvettes with dye solution (V = 3.5 mL and C = 2.0×10^{-5} M). After 12 h in the dark, the solution was replaced by MB solution (C = 1.0×10^{-5} M). Samples with dye solution were exposed to UVA irradiation (18 W lamp, 340–395 nm range) and Vis light (77 W tungsten halogen lamp, range of 350–2200 nm). Absorbance was measured at 664 nm for MB and 590 nm for CV (Metertech SP-830 PLUS, Metertech, Inc., Taipei, Taiwan) every 7 h during 38 h of irradiation. The percentage of MB decolorization caused during photodegradation was calculated using the same equation as the adsorption capacity [54]. Linear changes of the studied dyes' concentration in time (zero-order kinetics) allowed for the assumption that the dye concentration does not affect the monitored process in the studied reaction time, as the process rate reached its maximum in the applied conditions. Thus, calculation of the observed rate constants can be performed with a simple equation after the following mathematical transformations:

$$-\frac{dc_{dye}}{dt} = k \quad (2)$$

$$dc_{dye} = -kdt \quad (3)$$

$$c_t - c_0 = -kt \quad (4)$$

$$c_0 - c_t = kt \quad (5)$$

Taking into account the definition of the dye decolorization percentage, the above equation can be transformed as follows:

$$\% \text{ dye decolourization} = \frac{c_0 - c_t}{c_0} 100\% = \frac{kt}{c_0} 100\% = \frac{100\%k}{c_0} t = k_{obs} t \quad (6)$$

Application of the same starting concentration of the used dyes (c_0) allows for estimation of the relative photoactivity of the studied materials and their mutual comparison.

2.6. Electron Paramagnetic Resonance (EPR) Spectroscopy

EPR measurements were performed on an X band EPR SE/X-2541M spectrometer (Radiopan, Poznań, Poland) with 100 kHz modulation. The microwave frequency was monitored with a frequency meter. The magnetic field was observed with an automatic NMR-type JTM-147 magnetometer (Radiopan, Poznań, Poland). Measurement conditions were as follows: microwave frequency: ca. 9.33 GHz (X-band); microwave power: 2–58 mW; modulation amplitude: 0.12–1 mT; sweep: 10–100 mT; sweep time: 4 min; time constant: 0.1 s; receiver gain: 0.3–8.0 × 10^5. Spectra of complexes (**2**)–(**5**) were registered for powdered samples and composites.

3. Results

The structural compatibility and purity of the synthesized complexes (**1**)–(**5**) were verified using spectroscopic methods. However, it should be noted that ^{13}C NMR spectra for complexes (**4**) and (**5**) were not recorded, as Ru(III) compounds are paramagnetic, which limits the applicability of this technique [59]. The obtained powdered samples of the studied compounds were introduced in a poly(methyl methacrylate) (PMMA) matrix to create composite systems that were subsequently subjected to further investigations.

3.1. Characterization of PMMA + Complex Composites

The obtained compounds and their composites were analyzed using solid-state UV-Vis diffuse reflectance spectroscopy (UV-Vis DRS). The HOMO–LUMO energy gap of powders (**1**)–(**5**) was determined using the Kubelka–Munk (K-M) function plotted against light energy (i.e., K = f(hν), where K = $(1-R)^2/2R$ and R is the reflection). In the case of TOCs, the HOMO–LUMO gap is 3.12 eV, 2.96 eV, and 2.39 eV for (**1**) (Figure 1a), (**2**) [31], and (**3**) [31], respectively. In turn, for ruthenium complexes, it is 2.75 eV and 2.78 eV for (**4**) and (**5**), respectively (Figure 1b). Analysis of spectral data revealed that λ_{max} was 308 nm (**1**) (Figure 1c), 306 nm (**2**) [31], 330 nm, 395 nm (**3**) [31], and 334 nm (**4**), (**5**) (Figure 1d). The maximum absorption was also determined for the composite materials.

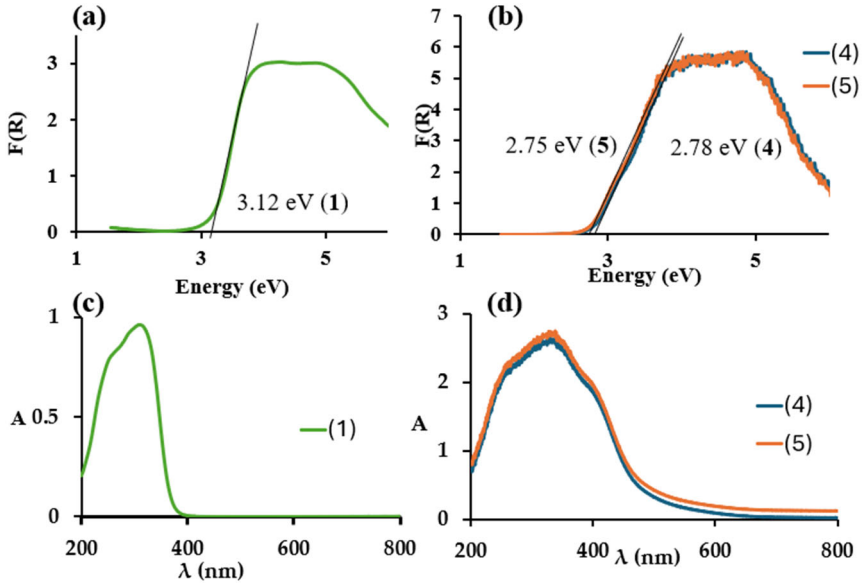

Figure 1. The results of studies on micro-grains (**1**), (**4**), and (**5**), carried out using UV-Vis diffuse reflectance spectroscopy (DRS) to investigate their optical properties (**a**,**b**), are presented together with the determination of the HOMO–LUMO gap for these compounds, derived from Kubelka–Munk function plots versus light energy (**c**,**d**).

Samples containing complex (**1**) (2% and 5% by weight) exhibited two maxima at 236 nm and 281 nm (Figure 2a), corresponding to the absorption maxima of PMMA. The PMMA + (1) 20 wt.% composite showed a broad absorption range (200–450 nm) with a low-intensity band peaking at approximately 330 nm. In the case of the PMMA + (**2**) series, the absorption edge is slightly shifted toward the visible light range (400 nm for PMMA + (**2**) 2% and 5%, and 480 nm for PMMA + (**2**) 10% and 20%) (Figure 2b). However, for the PMMA + (**3**) composites, the absorption edge is positioned at 480 nm for PMMA + (**3**) 2% and 5% samples and 500 nm for PMMA + (**3**) 10% and 20%. The absorption maximum remains in the ultraviolet range (Figure 2c).

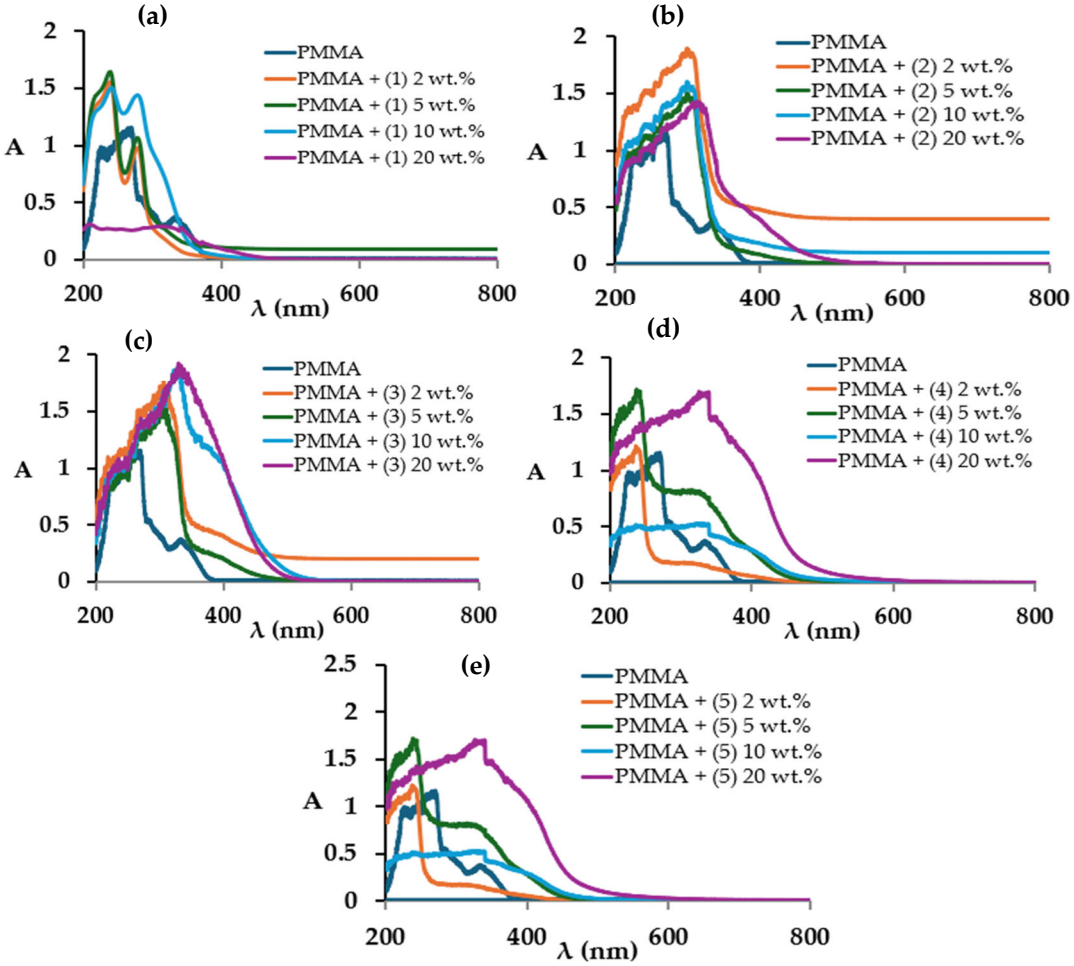

Figure 2. Solid-state UV-Vis-diffuse reflectance spectra (DRS) of the composites PMMA + (**1**)–(**5**) (**a**–**e**).

Composite materials made of PMMA and ruthenium complexes are characterized by an absorption edge in the 400–450 nm range. Almost all samples have two maximum absorptions in the 238–336 nm range (λ = 236–281 nm PMMA range). The exception is the PMMA + (**5**) 20 wt.% sample, where the absorption edge is located around 550 nm and one of the maximum absorptions was found at 420 nm (Figure 2d,e).

Composite materials based on poly(methyl methacrylate) containing 2%, 5%, 10% and 20% of complexes (**1**)–(**5**) were spectrally characterized to confirm the presence of the complex and that the structure of the compound does not change after introduction into the polymer matrix (Figure 3). Previously, our research exhibited that the structures of titanium–oxo complexes (**1**)–(**3**) are stable in contact with water. IR spectra and XRD diffractograms did not register significant differences [31,32].

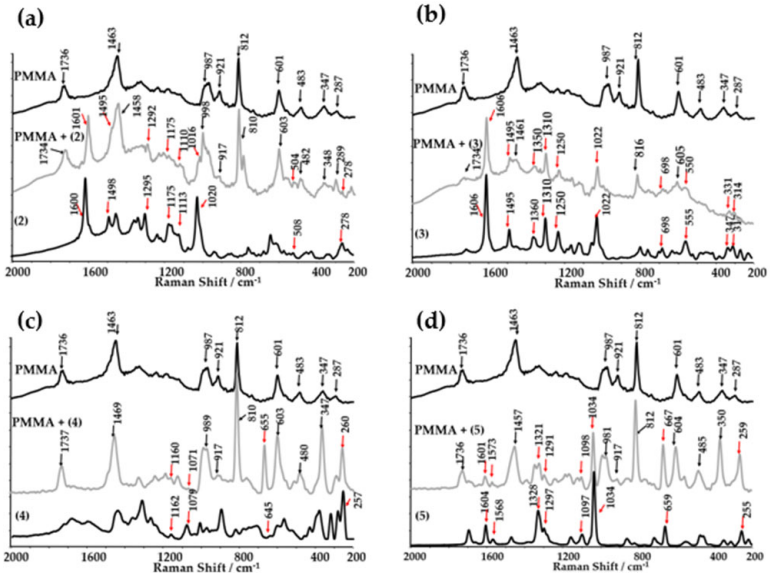

Figure 3. Raman spectra of powders (**2**) (**a**), (**3**) (**b**), (**4**) (**c**), and (**5**) (**d**), their composites containing 20 wt.% of the complex, and pure PMMA.

The analysis of scanning electron microscope (SEM) images provided insights into the dispersion of complexes (**1**)–(**5**) within the polymer matrix (Figures S1 and S2). The PMMA + (**1**) and PMMA + (**2**) composite samples are comparable, containing grains with diameters between 60 and 200 nm. Their high surface energy promotes aggregation, forming 30 to 250 μm grains. The packing density of these aggregates increases with the wt.% concentration of the complexes in the PMMA matrix. In the PMMA + (**3**) sample, densely packed crystalline grains are observed, with sizes dependent on the complex concentration in the matrix. At lower concentrations (2 wt.% and 5 wt.%), the sample primarily comprises grains with diameters between 145 and 355 nm and occasional larger grains measuring 200 to 500 μm. At higher concentrations (10 and 20 wt.%), the samples contain microcrystals of the oxo complex ranging from 900 nm to 5 μm in size (Figure S1).

The morphology of composite samples enriched with complexes (**4**) and (**5**) resembles that of the composites containing complexes (**1**) and (**2**). These composites are formed by dispersed grains with diameters of 40–200 nm, which, depending on concentration, may form larger micrometric aggregates (Figure S2). Additionally, SEM-EDX analysis confirms the presence of complexes (**2**)–(**5**) in the composite samples (Figures S3 and S4, Table S1), while the presence of complex (**1**) grains in the PMMA composites was verified in a previous SEM-EDX study [32].

A crucial aspect of our study was confirming that the investigated complexes retained their structure after being incorporated into the polymer matrix. To this end, we recorded Raman spectra of pure PMMA, complexes (**2**)–(**5**), and PMMA + ((**2**)–(**5**)) composites. Analysis of the spectra confirmed that the introduction of the studied complexes into the PMMA matrix did not significantly alter their structure (Figure 3). Key to this identification were the bands observed around 1600 cm^{-1} (ν_{as}(COO)), which confirm the coordination of the carboxylate group within the α-hydroxycarboxylate ligand. Additionally, the detection of ν(O-CR) bands between 1200 and 1000 cm^{-1} indicates the presence of coordinated alkoxide groups characteristic of the TOCs' structure. Weak bands appearing below 900 cm^{-1} further suggest the presence of titanium–oxo bridges. The structural stability of complex (**1**) in the PMMA + (**1**) composite had been previously confirmed [37]. In the Raman spectra of composites containing ruthenium(III) complexes, bands around 1600 cm^{-1} were observed, confirming the coordination of ligands. Moreover, bands in the range of 1320–650 cm^{-1}

were attributed to (CN) group vibrations, while the band near 260 cm^{-1} corresponds to ν(Ru-O) vibrations.

X-ray Absorption Near-Edge Structure (XANES) spectroscopy, utilizing synchrotron radiation, was employed to confirm the structure of complexes (**1**)–(**3**) in the composite samples. This technique involves photon absorption, where core-level electrons are excited to unoccupied states when the photon energy meets or exceeds the binding energy. The absorption edge, corresponding to the core-level energy specific to each element, makes XANES an element-selective method. Titanium L-edges are rarely studied in complex titanium clusters. The discussion of electronic structures is difficult because the observed pattern depends on crystal field splitting, spin–orbit coupling, and charge transfer effects. Also, in a theoretical approach, multiplet interactions affect the Ti L-edge spectrum [60]. However, it is known that peak numbers and their positions and profiles depend strongly on the local environment. Lätsch et al. discussed in detail XAS spectra of several Ti(IV) complexes, among them $[Ti_2O_2(acac)_4]$ with bridging oxo ligands. They showed that it significantly differs from tetrahedral mononuclear complexes, and four main features are observed.

Nevertheless, the described complexes did not exceed the dimer. We decided to apply the XANES method for Ti L-edges for the complicated cores observed in our structures. The energy range for titanium was carefully selected to avoid the edge regions of other elements, which is crucial for proper spectra normalization. Two detection modes were also used, differing in penetration depth; the TEY detector reaches tens of nanometers, whereas the fluorescence yield (FY) detector can go up to several hundred nanometers [61]. Signals of a powder from TEY and FY detectors are comparable, and only TEY results will be presented. For composites, the TEY detector cannot provide any signal, and so results from the FY detector will be given. The L-edges of 3*d* transition metals have been relatively underexplored, partly due to their significant surface sensitivity. These edges are highly responsive to variations in coordination and oxidation states and, owing to their reduced intrinsic broadening, provide more detailed insights into the electronic structure of transition metal ions.

The spectra for titanium significantly differ in peak position. For powders, two additional tiny features in the pre-edge region were identified (at. ca. 456.4 and 457.3 eV), resulting from dipole forbidden transitions (Figure 4).

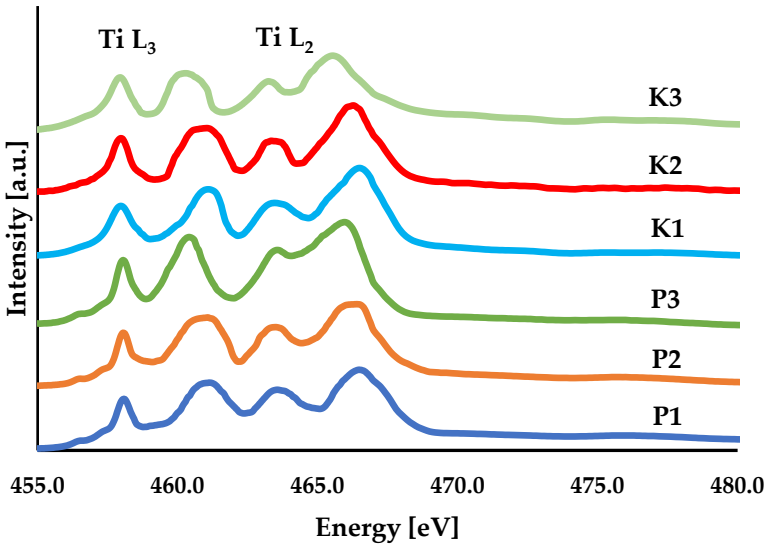

Figure 4. Normalized XANES spectra of titanium(IV) $L_{2,3}$-edge for powdered samples (P1, P2, P3) collected using the TEY detector and composite materials (K1, K2, K3) with 20% admixture of the studied titanium complexes using an FY detector.

Such signals in the range of 456.5–457.5 eV were also observed for TiO_2 [62,63]. They are not visible for our composites registered in FY mode. It should be noted that the spectra were successfully measured only for the composites with the highest admixture of the studied titanium complex (20%). After dispersing our complexes in a polymeric matrix, those spectra underwent no significant changes, and the shifts are within 0.3 eV. This might indicate the stability of the obtained cores. In all cases, titanium spectra show more intense bands corresponding to the L_2 edge than for the L_3 peaks. In general, there are four main features (Table S2). Peaks at ca. 458 and 461 eV correspond to $2p_{3/2} \rightarrow t_{2g}$ and $2p_{3/2} \rightarrow e_g$ transitions, whereas at ca. 463 and 466 eV they correspond to $2p_{1/2} \rightarrow t_{2g}$ and $2p_{1/2} \rightarrow e_g$, respectively. It should be noted that we cannot distinguish any significant profile change or band splitting for e_g levels. This effect is quite common, even for TiO_2, and it is ascribed to the splitting of e_g levels into d_{z^2} and $d_{x^2-y^2}$, and the profile change is considered a fingerprint between rutile and anatase [63]. In the reported spectra, a deconvolution was performed in Athena using Gaussian functions, and the results are presented in Table S2. In the case of FY detection mode, the spectra were much noisier, and hence they were smoothed. Nevertheless, no obvious pre-peak was observed, and smoothing did not exclude any peak. The profound structural and topological differences concerning even coordination numbers for the studied titanium complexes resulted in peak position shifts. The separation between t_{2g} and e_g levels is called crystal field splitting (Δ parameter). Hence, we can calculate this parameter from L_3 and L_2 edges. In our case, this difference is similar for both edges, being 3.0 and 3.0 for P1, 2.9 and 2.8 eV for P2, 2.3 and 2.4 eV for P3, 3.1 and 3.1 for K1, 3.0 and 3.0 for K2, and 2.3 and 2.2 eV for K3. Hence, we can suppose that both core holes ($2p_{3/2}$ and $2p_{3/2}$) are screened similarly. These data also show that Δ_{oct} (almost all titanium atoms were found in an octahedral environment, except for Ti4 in (**1**) and Ti2 in (**2**) [31,32]) for powders and composites are almost identical, and the changes are tiny (up to 0.2 eV). It also proves that the polymeric matrix did not affect the structure of titanium clusters. Moreover, these data agree well with those determined using the Kubelka–Munk method and theoretical calculations, which were 3.12, 2.96, and 2.39 eV for (**1**), (**2**), and (**3**), respectively [32].

Unfortunately, XANES experiments have only been conducted on titanium complexes, which is primarily due to sample availability and the characteristics of the beamline. Our spectra were measured using soft X-ray radiation, with 2000 eV as the maximum available energy at the PIRX beamline. This setup is ideal for probing 3d transition metals at their L-edges but is far less effective for 4d metals; for ruthenium, only the M-edge would be accessible. This limitation is supported by numerous studies on L-edges of first-row transition metals, with far fewer publications addressing the M-edges of ruthenium.

*3.2. Cationic Dyes' Adsorption on Composites PMMA + ((**1**)–(**5**))*

The adsorption capacity of the tested composites was evaluated to measure their effectiveness in removing dye contaminants from water. Cationic dyes—methylene blue (MB), rhodamine B (RhB), and crystal violet (CV)—were selected as model contaminants. The results in Figure 5 and Table S3 reflect 24 h of interaction between the composites and the dye solutions without light. In interpreting the received results, we considered (i) the effect of the complex type on the adsorption of model dyes and (ii) the impact of varying complex concentrations within the composite samples. Generally, it was noted that the oxo–Ti(IV) complexes showed superior adsorption of MB compared to the other dyes, while the Ru(III) complexes more effectively adsorbed CV. Both types of complexes demonstrated low adsorption of RhB (Figure 5). The amount of adsorbed dye increased with rising complex concentration (Table S3). The composite enriched with complex (**3**) exhibited the highest adsorption, while the dye adsorption levels of composites containing

the remaining complexes were relatively similar, remaining below 11% even at 20 wt% complex content.

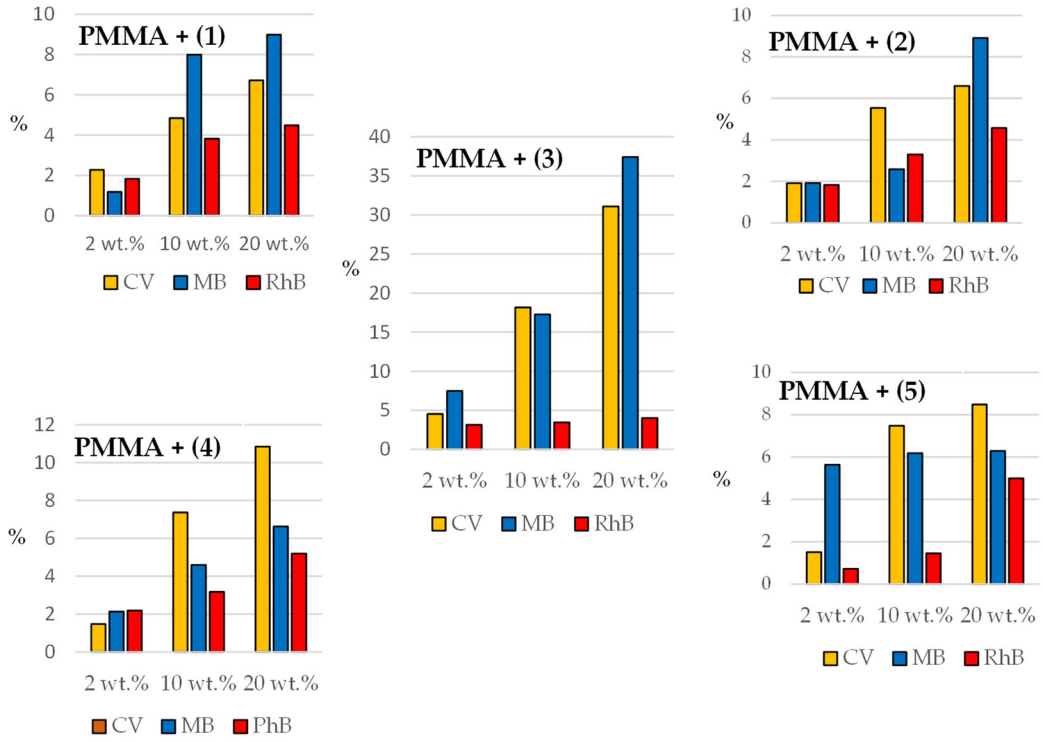

Figure 5. Percentage reduction of the concentration of the studied group of dyes by PMMA composites with complexes (**1**)–(**5**). For clarity, results are shown for systems containing 2, 10, and 20 wt.% of complexes; complete data are provided in Table S3.

*3.3. Estimation of Photocatalytic Activity of Composites PMMA + ((**1**)–(**5**))*

The photocatalytic activity of composites containing titanium(IV)–oxo complexes and ruthenium(III) complexes was assessed by monitoring changes in the decolorization of MB and CV solutions under UV irradiation and MB under visible light (Vis) (Figures S5–S7 and Tables S4–S6). The study focused on MB and CV dyes, as these were the most readily absorbed by the tested composites. Figure 6 presents representative changes in the decolorization percentages of MB (Vis and UV) and CV (UV) using the PMMA + (**3**) composite.

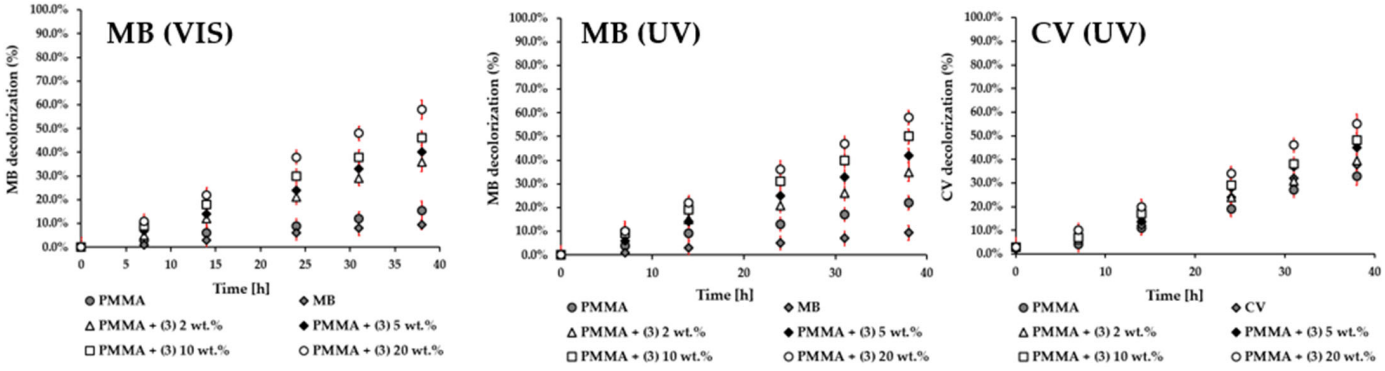

Figure 6. Changes in the percentage of dye decolorization over time for MB (VIS and UV) and CV (UV) with PMMA + (**3**) composite, as an example.

Figure 7 illustrates the changes in the observed rate constants (h^{-1}) for MB solution decolorization relative to PMMA for PMMA + (**1**)–(**5**) composites exposed to Vis and UV light (measurement data provided in Figures S5 and S7 and Tables S4 and S6). Meanwhile,

Figure 8 presents the results of the study of changes in the rate constants (h^{-1}) for CV solution decolorization under UV light for the tested group of composites (measurement data provided in Figure S6 and Table S5). The decrease in the concentration of both dyes during irradiation follows a linear trend consistent with zero-order kinetics, indicating that the photodecomposition rate of each dye remains constant throughout the measurement period. The analysis of the results indicates that the composites enriched with oxo–Ti(IV) complexes (**1**) and (**2**) exhibited the highest photocatalytic activity under UV light. Among these, the PMMA + (**2**) composites stand out for their exceptional performance, achieving the highest percentage of MB solution decolorization across all tested concentrations (2–20 wt.%), with values ranging from 45.3% to 73.1%, significantly outperforming the PMMA control (17.4%) (Table S4).

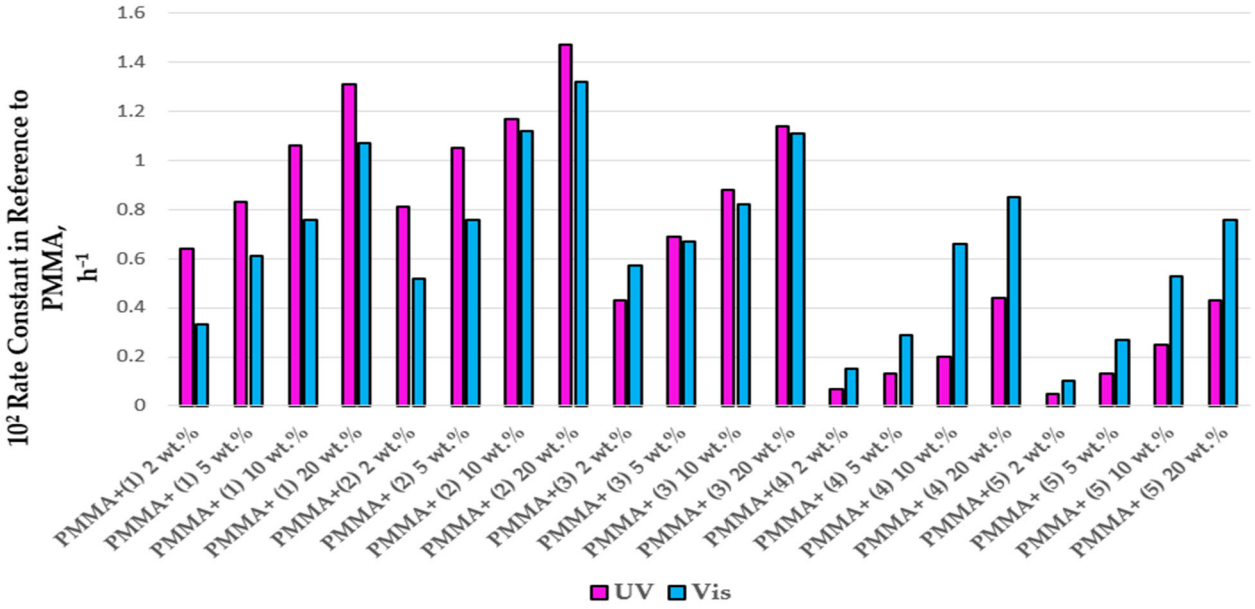

Figure 7. Changes in the observed rate constants (h^{-1}) of MB solution decolorization processes relative to PMMA for composites PMMA + (**1**)–(**5**) exposed to UV and visible (Vis) light.

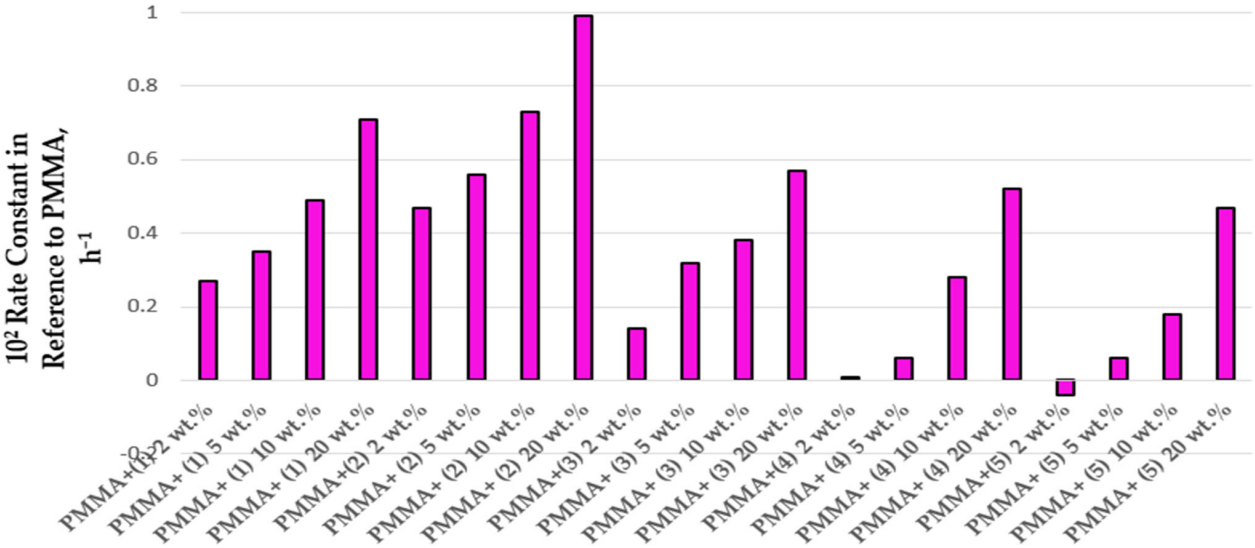

Figure 8. Changes in the observed rate constants (h^{-1}) of CV solution decolorization processes relative to PMMA for composites PMMA + (**1**)–(**5**) exposed to UV light.

This superior activity is further corroborated by the decolorization studies on CV solutions, where the PMMA + (**2**) samples with 2–20 wt.% of the complex achieved a decolorization degree between 51.1% and 70.9%, compared to 37.5% for pure PMMA. In contrast, the oxo complex (**3**) and Ru(III) complexes (**4**) and (**5**) showed markedly lower photocatalytic efficiencies. Notably, for all composites, the photocatalytic activity was consistently improved with increasing concentrations of the complexes in the PMMA matrix. However, it should be emphasized that the composites containing Ru(III) complexes did not exhibit any photocatalytic activity at the lowest concentration tested (2 wt.%) in the decolorization of CV solutions (Figures 8 and S6).

The studied samples were also irradiated with visible light (Vis) to assess their effect on the decolorization of MB solutions. The results of these measurements are presented in Figure 7 and Figure S7, as well as Table S6. Subsequently, these experiments were repeated over three cycles to verify the stability of the photocatalytic activity of the tested systems. The findings demonstrated that the photocatalytic activity of the studied samples remained consistent across all measured cycles (Figure 9). The results of our investigations revealed that composites containing complexes (**1**) and (**2**) exhibited lower photocatalytic activity under visible light compared to their activity under UV radiation (Figure 7). However, the composite containing complex (**3**) as a filler showed a significant increase in activity under visible light, nearing the activity observed under UV exposure (Figure 7 and Table S6). In contrast, both composites containing Ru(III) complexes (PMMA + (**4**) and PMMA + (**5**)) displayed notable activity under visible light. Additionally, it is worth emphasizing that in all samples, the concentration of the complex within the polymer matrix played a crucial role in determining their photocatalytic activity.

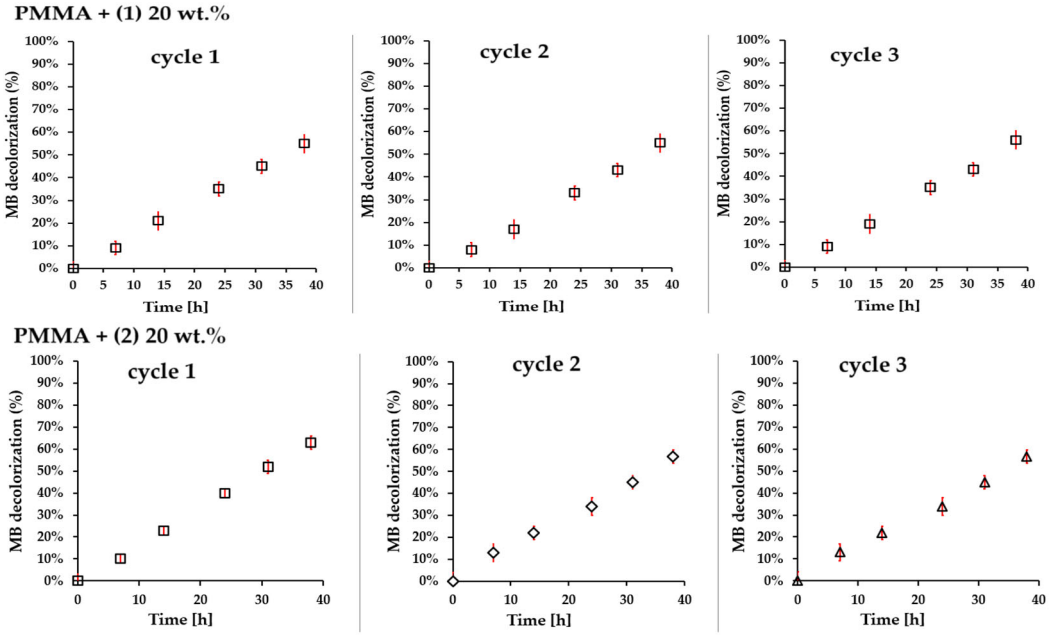

Figure 9. *Cont.*

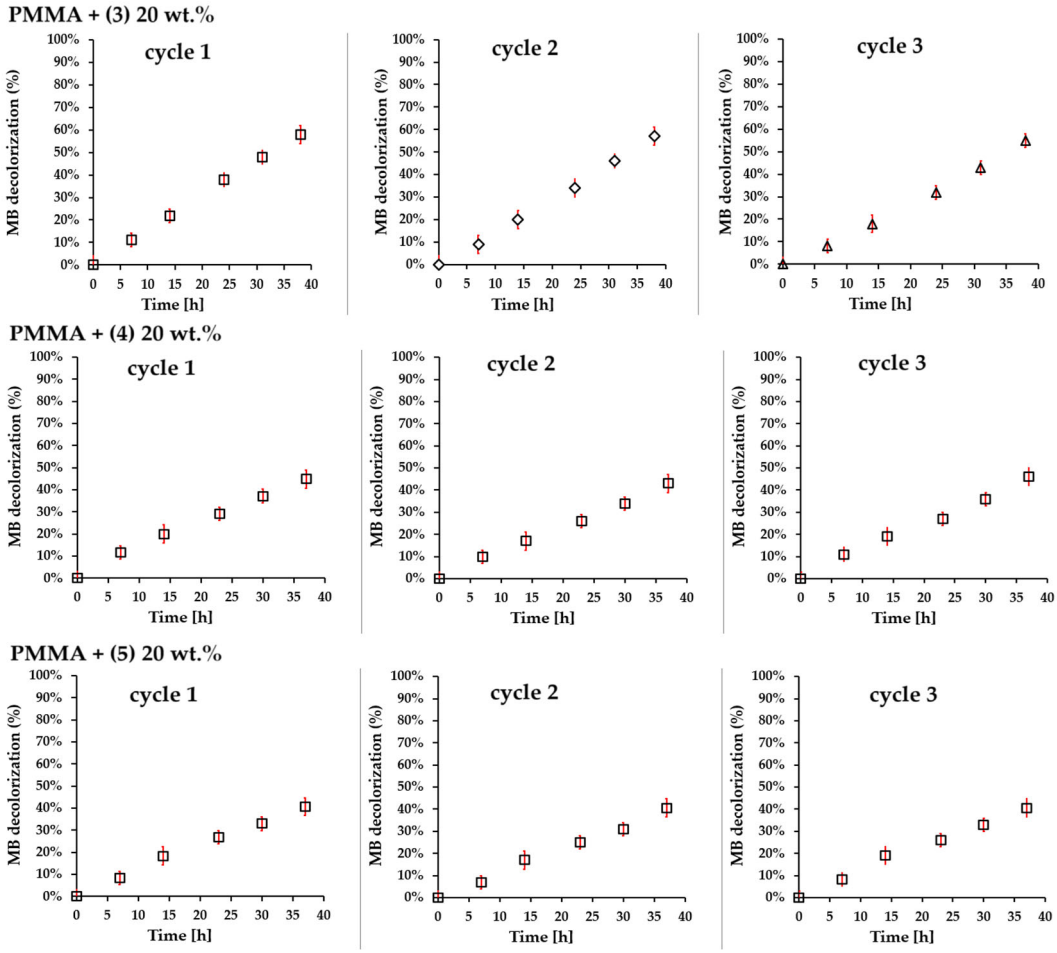

Figure 9. Recycling MB decolorization tests of composite materials PMMA + Comp. 20 wt.% (Comp. = (**1**), (**2**), (**3**), (**4**), and (**5**)) irradiated with visible light.

3.4. Electron Paramagnetic Resonance (EPR) Spectroscopy

EPR spectroscopy confirmed the presence of paramagnetic species in all tested complexes and their composites, while no signals were detected in the spectra of pure PMMA. Upon daylight activation, complex (**1**) generated O_2^- and Ti(III) species, while its PMMA composite also contained O^- [32]. Complexes (**2**) and (**3**) exhibited different behaviors, as (**2**) showed a free electron signal, whereas (**3**) produced O^-, O_2^-, and Ti^{3+} species, which were also present in samples of both composites (Table S7, Figures S8 and S9). Analysis of ruthenium(III) complexes' spectra revealed that (**5**) generates a significantly more intensive signal than complex (**4**). In the case of both powders and composites, signals from Ru(III) were recorded, but in the case of composites, they are much weaker (Table S7, Figures S10 and S11). These results support the proposed photocatalytic mechanisms by confirming that photoactivation generates reactive paramagnetic species, which play a crucial role in catalytic processes.

4. Discussion

The conducted studies focused on evaluating the photocatalytic activity of Ti(IV)–oxo complexes stabilized with α-hydroxycarboxylic ligands, which were incorporated into a PMMA matrix. The compounds studied included $[Ti_8O_2(O^iPr_{)20}(man)_4]$ (**1**), $[Ti_4O(O^iPr)_{10}(O_3C_{14}H_8)_2]$ (**2**), and $[Ti_6O_4(O^iPr)_2(O_3C_{14}H_8)_4(O_2CEt)_6]$ (**3**), which had been structurally and spectroscopically characterized in our earlier research [31,32]. Additionally, composites containing K[Ru(Hedta)Cl]·$2H_2O$ (**4**) and $[Ru(pic)_3]\cdot H_2O$ (**5**) were investigated.

These Ru(III) complexes were synthesized via reactions of aquapentachlororuthenate(III) hydrate or ruthenium(III) chloride with EDTA or picolinic acid [38,64].

One of the aims of this research was to determine the possibility for the fabrication of surface-active composite coatings of the PMMA + Comp. type (Comp. = TOCs or Ru(III) complexes). The formation of such systems was crucial to protecting the structure of the studied compounds from hydrolysis or dissolution processes and minimizing nanograin aggregation. It is noteworthy that previous studies on the photocatalytic activity of TOCs primarily involved powdered forms. Thus, a significant stage of the research was confirming the structure of complexes (**1**)–(**5**) after their incorporation into the PMMA matrix. A comparison of the Raman spectra for complexes (**1**)–(**5**) and the PMMA + (**1**)–(**5**) composites revealed that embedding these complexes into the PMMA matrix did not induce significant structural changes. For multinuclear oxo-Ti(IV) complexes (**1**)–(**3**), the stability of their structure within the composite was further confirmed through XAS studies.

In the initial stage of the study, we aimed to determine how the introduction of Ti(IV) or Ru(III) complexes into a polymer matrix influences the adsorption of organic dyes. Most of the insights into the sorption properties of Ti(IV) and Ru(III) compounds come from studies on metal–organic frameworks (MOFs) [65–70], which are valued for their high porosity, structural diversity, and highly active dye adsorption sites [71–73]. The amount of dye adsorbed depends on the dye's structure and is influenced by the electron density of the adsorbents [74]. For example, MB and CV molecules are smaller than RhB, allowing more of them to interact with TOCs or Ru(III) complexes.

In our previous work, we demonstrated that introducing an additional ligand into the structure of compound (**3**) increases the electron density due to chelate rings and free carboxyl groups [31]. In contrast, compound (**2**) contains significantly fewer electron-dense areas. We hypothesize that electron-dense regions attract dye molecules, as the positively charged nitrogen in the dye structure is generally inclined to interact with electron-rich surface groups [75]. Molecular electrostatic maps of mandelic acid suggest that the hydroxyl group is most susceptible to nucleophilic attack [76,77]. However, in compound (**1**), this hydroxyl group is coordinated, potentially reducing the electron density. For Ru(III) complexes containing EDTA and picolinate ligands, the highest electron density is expected in the C=O groups [78,79]. This effect aligns with studies on EDTA-containing copper complexes, where the C=O groups exhibit high electronegativity, while the rest of the molecule remains neutral [78]. The reduced adsorption efficiency of Ru(III) complexes, especially compared to titanium compounds, such as (**3**), may be attributed to their smaller size, which limits the electron-dense surface area available for interactions with dye molecules.

Basing on the obtained results, the next stage of our study focused on the use of methylene blue (MB) and crystal violet (CV) solutions. To evaluate the photocatalytic activity of the studied complexes (1)–(5), it was crucial to determine their maximum absorption within the composite materials as well as their HOMO–LUMO gap values. These parameters can be tailored to achieve desired properties, for instance, through structural modifications of the complexes, such as functionalizing the stabilizing ligands. Liu et al. demonstrated that introducing salicylate ligands can reduce the Ep values of complexes from 2.24 to 1.88 eV [80], while chromophore ligands broaden this range from 3.41 to 1.98 eV [81]. For ruthenium compounds, the existing literature suggests that modifications to the HOMO–LUMO gap are primarily focused on Ru(II) complexes, particularly those containing bipyridine ligands. Adjusting the position of the bipyridine substituent or altering the halide coordination can result in either an increase or decrease in the HOMO–LUMO gap [82,83]. Similar trends are expected to apply to Ru(III) complexes; however, these compounds have been studied less extensively. Among the tested Ru(III) compounds, complexes (**4**) and (**5**) exhibit comparable Ep values of 2.75 and 2.78 eV, respectively, placing

them between studied complexes (**2**) (Ep = 2.96 eV) and (**3**) (Ep = 2.39 eV). This suggests that these complexes are also likely to exhibit photocatalytic activity [84,85].

The photocatalytic activity of the studied composites containing 2, 5, 10, and 20 wt.% of complexes (**1**)–(**5**) was assessed by analyzing the decolorization of MB solution samples irradiated with UV and visible (Vis) light, following the ISO 10678 standards [86]. Additionally, tests in UV was carried out using CV solutions.

The performed tests confirmed that some percentage of each studied dye is adsorbed on the composite surface (Table S3). To maintain the same concentration condition in each kinetic run, during photodegradation tests, the "old" dye solution was replaced after the adsorption process with a fresh one. Thus, the starting dye concentration during each kinetic run was the same. This is important considering the equation used for calculation of the observed rate constants (Equation (6)), where k_{obs} is defined as

$$k_{obs} = \frac{100\%k}{c_0} \quad (7)$$

As a measure of a dye concentration, the percentage of dye decolorization was used. Because both of these parameters are inversely proportional to each other, the observed linear dependencies for decolorization vs. time increase, although the dye undergoes decomposition. Application of the change in the solution color during the photodegradation of MB and CV is based on the mechanism of their photodecomposition, studied earlier [5,87,88].

Paths of MB photodegradation have been studied for years [5,87–89]. The process can be studied spectrophotometrically because a blue, oxidized form of MB in a reaction with reactive oxygen species, mainly $^{\bullet}OH$, generated on a photocatalyst surface forms colorless photodegradation intermediates [87]. The decolorization is caused by breaking of the MB central aromatic ring [5]. The further decomposition of the intermediates continues until CO_2, H_2O, and other inorganic ions are formed as final photodegradation products [5,87]. Moreover, spectrophotometric MB photodegradation is a kind of reference process, being involved in the norm ISO 10678:2024 (formerly ISO 10678: 2010) [86,90].

Photodegradation of CV proceeds similarly. A free electron generated during composite irradiation reacts with water molecules on the composite surface, producing different ROS. This process, i.e., the water splitting reaction, in fact, is crucial for the whole photodegradation process here and in other, similar photodegradation reactions [91]. One of the most common ROS in aqueous systems is hydroxyl radical [87,91,92]. It reacts with CV molecules, making it fragment into colorless species [92], and it finally produces simple inorganic molecules [93]. Processes of N-demethylation and oxidative degradation are placed among the first steps of CV photodegradation [93,94].

The monitored decolorization of MB and CV aqueous solutions is related to the first step of a particular dye's photodecomposition. This procedure is commonly used in the photoactivity tests [5,86–94] because of its simplicity (spectrophotometric studies, the zero-order or first-order kinetic equations) and sensitivity (e.g., significant changes of absorption). Among the tested dyes, MB solutions showed the highest photocatalytic degradation efficiency, as well as MB's susceptibility to light-induced breakdown under both UV and visible light irradiation [95]. The highest rate constant for the photoinduced decolorization process was observed in UV-irradiated PMMA + (**2**) samples, where the per cent of MB decolorization increased from 33.6% to 63.6% as the complex concentration dose rose from 2 to 20 wt.% (Figure 7, Table S4). The tested composites can be classified by their activity profile as follows: (i) composites mainly active in the UV range, enriched with complexes (**1**) and (**2**); (ii) composites active under visible light, containing complexes (**4**) and (**5**); and (iii) a composite showing activity in both UV and visible light ranges, incorporating complex (**3**). In the systems evaluated, oxo–Ti(IV) complexes demonstrated the greatest photocatalytic

activity. Findings from previous structural studies of complexes (**1**)–(**3**) [31,32] and their physicochemical properties suggest that the stabilizing carboxylate ligand type is the primary factor impacting their photocatalytic activity. Complexes (**1**) and (**2**), stabilized by α-hydroxycarboxylic ligands (mandelate or 9-hydroxy-9-fluorenecarboxylate), exhibited relatively large HOMO-LUMO energy gaps of 3.12 eV and 2.96 eV, respectively, accounting for their strong UV activity, which is confirmed by the rate constants of the photoinduced decolorization of MB and CV solutions. In contrast, complex (**3**), stabilized by 9-hydroxy-9-fluorenecarboxylate and propionate ligands, has a reduced E_p value of 2.39 eV, resulting in lower UV activity but increased visible light activity. The PMMA + (**3**) composite (2 wt.%) showed superior activity in the visible light range compared to the UV range. It slightly decreased with the complex concentration increase (Figure 6).

Ruthenium(III) complexes (**4**) and (**5**) exhibited generally lower photocatalytic activity compared to the Ti(IV)-based complexes (**1**)–(**3**). They were primarily active under visible light, likely due to their HOMO–LUMO energy gap values of 2.75 and 2.78 eV for (**4**) and (**5**), respectively. The reduced activity of the Ru(III) complexes may be attributed to their photocatalytic mechanism, which involves the reduction of Ru(III) to Ru(II). In aqueous solutions, this reduction produces H_2O_2 molecules that subsequently form hydroxyl radicals [96,97]. The lower reactivity of Ru(III) complexes suggests that they generate fewer hydroxyl radicals compared to the number of reactive oxygen species (ROS) produced by Ti(IV)–oxo complexes stabilized with α-hydroxycarboxylate ligands. These results indicate that, in this case, the type of ligand also affects the activity differences observed between complexes (**4**) and (**5**).

The photocatalytic mechanism involves the excitation of electrons from the valence band to the conduction band upon irradiation with light of an appropriate wavelength, leading to the formation of electron–hole pairs. These species interact with oxygen or water, generating reactive oxygen species (ROS), which drive photocatalytic reactions [84]. In metal complexes, electron transfer occurs between the HOMO (ligand) and LUMO (metal center, Ti or Ru) [29]. EPR spectroscopy was used to identify the ROS generated on the surface of the tested materials, helping to understand their photocatalytic behavior. The results indicate that the most effective material is the PMMA + (2) composite, as its EPR spectrum shows the least distortion, suggesting efficient charge transfer. Composites containing titanium oxo-clusters (TOCs) exhibit similar EPR patterns, with signals corresponding to O^-, $O_2{}^-$ radicals, and Ti^{3+} species, which are key contributors to photocatalysis [30]. Among the studied TOCs, (2) shows a distinct free electron signal, while (**1**) and (**3**) display typical features of Ti^{3+} and superoxide radicals, confirming their role in ROS generation [32,98]. For ruthenium(III) complexes, the EPR spectra indicate that Ru(III) centers are the only paramagnetic species present, with no ROS signals detected. This suggests that photocatalysis in these materials follows a different mechanism, likely involving Ru(III) reduction to Ru(II) upon irradiation. Because Ru(II) is diamagnetic, it does not produce an EPR signal, supporting the idea that electron transfer occurs within the ruthenium center rather than through ROS formation [85]. Notably, only the composite containing 20 wt.% of (5) exhibits a relatively intense signal, indicating a higher concentration of Ru(III) centers (Table S7 and Figures S9 and S10) [99]. These findings align with the observed photocatalytic activity trends, confirming that titanium-based composites primarily operate through ROS-mediated processes, while ruthenium-based materials rely on direct electron transfer mechanisms.

5. Conclusions

This study assessed the adsorption properties and photocatalytic activity of composite materials created by incorporating Ti(IV)–oxo complexes stabilized with α-hydroxy

carboxylate ligands ((**1**)–(**3**)) and Ru(III) complexes ((**4**) and (**5**)) into a PMMA matrix. Spectroscopic analyses (Raman and XAS) confirmed that introducing these complexes into the polymer matrix did not lead to significant alterations in their structures. Notably, the absorption maximum of the composites shifted toward the visible light range (from 221 and 281 nm for pure PMMA to 336 and 420 nm in the case of sample PMMA + (**5**) 20 wt.%), especially in samples containing 10 and 20 wt.% of the complexes, enhancing their potential responsiveness under visible light.

The adsorption properties were evaluated using three cationic dyes: methylene blue (MB), crystal violet (CV), and rhodamine B (RhB). The composites demonstrated the highest adsorption with MB (max 37%) and the lowest with RhB (max 5%), with PMMA + (**3**) exhibiting the greatest adsorption capacity, likely due to the high electron density of complex (**3**) (Table 1).

Table 1. Comparative table of PMMA composites with Ti(IV) and Ru(III) complexes (the presented data refer to composites containing 2 wt.% and 20 wt.% of the tested complexes).

Composite	Maximum Dye Adsorption (%) MB	Photocatalytic Activity MB (%)	EPR Signals	Light Activation Range
TOCs				
PMMA + (**1**)	2.27–8.99	38–69 (UV) 27–55 (Vis)	Moderate (O_2^-, Ti^{3+})	UV
PMMA + (**2**)	1.92–8.91	45–73 (UV) 34–64 (Vis)	Strong (O^-, O_2^-, Ti^{3+})	UV
PMMA + (**3**)	7.48–37.40	35–58 (UV) 36–59 (Vis)	Moderate (O^-, O_2^-, Ti^{3+})	UV + Vis
Ru(III) complexes				
PMMA + (**4**)	2.14–6.62	19–33 (UV) 18–45 (Vis)	Weak (Ru^{3+})	Vis
PMMA + (**5**)	5.63–6.69	17–32 (UV) 16–41 (Vis)	Weak (Ru^{3+})	Vis

The photocatalytic activity was assessed under both UV and visible light. The results showed that composites containing titanium complexes had higher photocatalytic activity (58–73% degradation of MB in UV light, 55–71% degradation of CV in UV light, and 55–63% degradation of MB in visible light) than those containing ruthenium complexes (32–33% degradation of MB in UV light, 49–52% degradation of CV in UV light, and 40–45% degradation of MB in visible light). Based on photocatalytic performance, the composites could be classified as (i) UV-active composites ((**1**) and (**2**)), (ii) composites active under visible light ((**4**) and (**5**)), and (iii) a composite active under both UV and visible light ((**3**)). The photocatalytic activity was directly influenced by the type of central ion and the stabilizing ligand (Table 1). Ti(IV)-based composites exhibited superior photocatalytic performance due to the ability of Ti(IV) to generate reactive oxygen species (ROS), which are essential for efficient photocatalysis. In contrast, Ru(III)-based complexes rely on redox cycling between Ru(III) and Ru(II) rather than ROS generation, resulting in lower photocatalytic efficiency. Additionally, the stabilizing ligands affected the electronic structure of the complexes, with certain ligands widening the HOMO–LUMO gap and enhancing UV activity, while others extended the activity into the visible range. Therefore, the type of central ion and the stabilizing ligand both play crucial roles in determining the photocatalytic behavior of the composites.

Future research should focus on investigating the use of alternative polymer matrices to better understand how the properties of the host material influence photocatalytic

performance. Additionally, evaluating the composites under real-world conditions, such as in wastewater treatment applications, will help assess their long-term stability and efficiency in handling complex pollutant mixtures. Further studies on the recyclability and reusability of the composites are also crucial for improving their practical applicability and ensuring their sustainability in industrial processes.

Supplementary Materials: The following supporting information can be downloaded at https://www.mdpi.com/article/10.3390/app15041679/s1, Materials: Synthesis procedures of complexes (**1**)–(**5**). Figure S1. SEM images of the composite films enriched with titanium(IV)–oxo complexes (yellow rings mark TOCs' grains); Figure S2. SEM images of the composite films enriched with ruthenium(III) complexes (yellow rings mark Ru(III) complexes' grains); Table S1. SEM EDX quantity data. All values are given in mass per cent (%); Figure S3. SEM EDX spectra of pure PMMA and composites containing titanium(IV)–oxo complexes (**2**) and (**3**); Figure S4. SEM EDX spectra of composites containing ruthenium(III) complexes (**4**) and (**5**); Table S2. Ti $L_{2,3}$ edge (two first features correspond to L_3 and two latter features correspond to L_2 edges). Pre-edge features were visible at ca. 456.4 457.3 eV for powdered samples and experiments performed in TEY mode; Table S3. Percentage reduction of dyes by composites PMMA + ((**1**)–(**5**)); Figure S5. Changes in the concentrations of the methylene blue (MB) solution as a function of time for composite materials PMMA + (**1**)–(**5**) 2–20 wt.% irradiated with UV light; Table S4. Decolorization percentages of MB solutions for the studied reactions relative to the composites irradiated by UV light; Figure S6. Changes in the concentrations of the crystal violet (CV) solution as a function of time for composite materials PMMA + (**1**)–(**5**) 2–20 wt.% irradiated with UV light; Table S5. Decolorization percentages of CV solutions for the studied reactions relative to the composites irradiated by UV light. Figure S7. Changes in the concentrations of the methylene blue (MB) solution as a function of time for composite materials PMMA + (**1**)–(**5**) 2–20 wt.% irradiated with Vis light; Table S6. Decolorization percentages of MB solutions for the studied reactions relative to the composites irradiated by VIS light. Figure S8. EPR spectra of the PMMA composites with (**2**) and of powdered TOC. Conditions: room temperature; microwave frequencies: 9.324675 GHz (PMMA+ (**2**) 2 wt.%), 9.324486 GHz (PMMA+ (**2**) 5 wt.%), 9.323992 GHz (PMMA+ (**2**) 10 wt.%), 9.323746 GHz (PMMA+ (**2**) 20 wt.%), and 9.317209 GHz ((**2**)); modulation amplitude: 1 mT; sweep: 20 mT; sweep time: 4 min; time constant: 0.1 s; receiver gain: 2×10^5 (composites) and 0.5×10^5 ((**2**)). Table S7. EPR data for the studied PMMA composites and powdered complexes. Figure S9. EPR spectra of the PMMA composites with (**3**) and of powdered TOC. Conditions: room temperature; microwave frequencies: 9.324157 GHz (PMMA+ (**3**) 2 wt.%), 9.324280 GHz (PMMA+ (**3**) 5 wt.%), 9.323349 GHz (PMMA+ (**3**) 10 wt.%), 9.322974 GHz (PMMA+ (**3**) 20 wt.%), and 9.324018 GHz ((**3**)); modulation amplitude: 1 mT; sweep: 20 mT; sweep time: 8 min (composites) and 4 min ((**3**)); time constant: 0.1 s; receiver gain: 4×10^5 (composites) and 5×10^5 ((**3**)). Figure S10. EPR spectra of the PMMA composites with (**4**) and of powdered complex. Conditions: room temperature; microwave frequencies: 9.325410 GHz (PMMA+ (**4**) 2 wt.%), 9.324910 GHz (PMMA+ (**4**) 5 wt.%), 9.325450 GHz (PMMA+ (**4**) 10 wt.%), 9.325550 GHz (PMMA+ (**4**) 20 wt.%), and 9.322220 GHz (**4**); modulation amplitude: 1 mT; sweep: 400 mT (composites) and 200 mT (**4**); sweep time: 8 min (composites) and 4 min (**4**); time constant: 0.1 s; receiver gain: 6.3×10^5 (composites) and 4×10^5 (**4**). Figure S11. EPR spectra of the PMMA composites with (**5**) and of powdered complex. Conditions: room temperature; microwave frequencies: 9.325300 GHz (PMMA+ (**5**) 2 wt.%), 9.325630 GHz (PMMA+ (**5**) 5 wt.%), 9.325390 GHz (PMMA+ (**5**) 10 wt.%), 9.325470 GHz (PMMA+ (**5**) 20 wt.%), and 9.323610 GHz (**5**); modulation amplitude: 1 mT; sweep: 500 mT; sweep time: 2 min (**5**) and 4 min (composites); time constant: 0.1 s; receiver gain: 3.2×10^5 (composites and (**5**)).

Author Contributions: Conceptualization, A.R., O.I. and B.K.; methodology, B.K, P.P., T.M., O.I., A.T. and A.K.; validation, R.v.E., P.P. and A.R.; formal analysis, P.P., A.K. and O.I.; investigation, B.K., T.M. and A.T.; resources, B.K.; data curation, B.K., A.T., O.I., T.M and P.P.; writing—original draft preparation, B.K. and P.P.; writing—review and editing, P.P., A.R., A.T., T.M., R.v.E. and A.K.; visualization, P.P., B.K., A.T. and T.M.; supervision, P.P. and R.v.E.; project administration, P.P.; funding acquisition, R.v.E. All authors have read and agreed to the published version of the manuscript.

Funding: This research was funded by the National Science Center (Grant No. 2020/37/B/ST4/01082).

Institutional Review Board Statement: Not applicable.

Informed Consent Statement: Not applicable.

Data Availability Statement: The raw data supporting the conclusions of this article will be made available by the authors upon request.

Conflicts of Interest: The authors declare no conflicts of interest.

References

1. Yan, X.; Feng, J.; Li, P.; Li, J.; Ren, B.; Gao, S.; Cao, R. Fast and Efficient Removal of Mercury Ions Using Zirconium-Based Metal–Organic Framework Filter Membranes. *Inorg. Chem. Commun.* **2021**, *131*, 108796. [CrossRef]
2. Al-Tohamy, R.; Ali, S.S.; Li, F.; Okasha, K.M.; Mahmoud, Y.A.-G.; Elsamahy, T.; Jiao, H.; Fu, Y.; Sun, J. A Critical Review on the Treatment of Dye-Containing Wastewater: Ecotoxicological and Health Concerns of Textile Dyes and Possible Remediation Approaches for Environmental Safety. *Ecotoxicol. Environ. Saf.* **2022**, *231*, 113160. [CrossRef]
3. Olisah, C.; Adams, J.B.; Rubidge, G. The State of Persistent Organic Pollutants in South African Estuaries: A Review of Environmental Exposure and Sources. *Ecotoxicol. Environ. Saf.* **2021**, *219*, 112316. [CrossRef]
4. Lellis, B.; Fávaro-Polonio, C.Z.; Pamphile, J.A.; Polonio, J.C. Effects of Textile Dyes on Health and the Environment and Bioremediation Potential of Living Organisms. *Biotechnol. Res. Innov.* **2019**, *3*, 275–290. [CrossRef]
5. Khan, I.; Saeed, K.; Zekker, I.; Zhang, B.; Hendi, A.H.; Ahmad, A.; Ahmad, S.; Zada, N.; Ahmad, H.; Shah, L.A.; et al. Review on Methylene Blue: Its Properties, Uses, Toxicity and Photodegradation. *Water* **2022**, *14*, 242. [CrossRef]
6. Zada, N.; Saeed, K.; Khan, I. Decolorization of Rhodamine B Dye by Using Multiwalled Carbon Nanotubes/Co–Ti Oxides Nanocomposite and Co–Ti Oxides as Photocatalysts. *Appl. Water Sci.* **2020**, *10*, 40. [CrossRef]
7. Li, J.; Huang, L.; Jiang, X.; Zhang, L.; Sun, X. Preparation and Characterization of Ternary Cu/Cu2O/C Composite: An Extraordinary Adsorbent for Removing Anionic Organic Dyes from Water. *Chem. Eng. J.* **2021**, *404*, 127091. [CrossRef]
8. Suman; Chahal, S.; Kumar, A.; Kumar, P. Zn Doped α-Fe_2O_3: An Efficient Material for UV Driven Photocatalysis and Electrical Conductivity. *Crystals* **2020**, *10*, 273. [CrossRef]
9. Khan, I.; Shah, T.; Tariq, M.R.; Ahmad, M.; Zhang, B. Understanding the Toxicity of Trinitrophenol and Promising Decontamination Strategies for Its Neutralization: Challenges and Future Perspectives. *J. Environ. Chem. Eng.* **2024**, *12*, 112720. [CrossRef]
10. Shan, Z.; Yang, Y.; Shi, H.; Zhu, J.; Tan, X.; Luan, Y.; Jiang, Z.; Wang, P.; Qin, J. Hollow Dodecahedra Graphene Oxide- Cuprous Oxide Nanocomposites With Effective Photocatalytic and Bactericidal Activity. *Front. Chem.* **2021**, *9*, 755836. [CrossRef]
11. Khan, I.; Rizwan Tariq, M.; Ahmad, M.; Khan, I.; Zhang, B. Strategically Coupled Tungsten Oxide-Zinc Oxide Photosystems for Solar-Driven Nerve Agent Simulant Degradation and Hydrogen Evolution. *Sep. Purif. Technol.* **2025**, *354*, 129078. [CrossRef]
12. He, X.; Yang, D.-P.; Zhang, X.; Liu, M.; Kang, Z.; Lin, C.; Jia, N.; Luque, R. Waste Eggshell Membrane-Templated CuO-ZnO Nanocomposites with Enhanced Adsorption, Catalysis and Antibacterial Properties for Water Purification. *Chem. Eng. J.* **2019**, *369*, 621–633. [CrossRef]
13. Xiao, M.; Wang, Z.; Lyu, M.; Luo, B.; Wang, S.; Liu, G.; Cheng, H.; Wang, L. Hollow Nanostructures for Photocatalysis: Advantages and Challenges. *Adv. Mater.* **2019**, *31*, 1801369. [CrossRef] [PubMed]
14. Saravanan, R.; Gracia, F.; Stephen, A. Basic Principles, Mechanism, and Challenges of Photocatalysis. In *Nanocomposites for Visible Light-Induced Photocatalysis*; Khan, M.M., Pradhan, D., Sohn, Y., Eds.; Springer Series on Polymer and Composite Materials; Springer International Publishing: Cham, Switzerland, 2017; pp. 19–40, ISBN 978-3-319-62445-7.
15. Krakowiak, R.; Musial, J.; Bakun, P.; Spychała, M.; Czarczynska-Goslinska, B.; Mlynarczyk, D.T.; Koczorowski, T.; Sobotta, L.; Stanisz, B.; Goslinski, T. Titanium Dioxide-Based Photocatalysts for Degradation of Emerging Contaminants Including Pharmaceutical Pollutants. *Appl. Sci.* **2021**, *11*, 8674. [CrossRef]
16. Schneider, J.; Matsuoka, M.; Takeuchi, M.; Zhang, J.; Horiuchi, Y.; Anpo, M.; Bahnemann, D.W. Understanding TiO_2 Photocatalysis: Mechanisms and Materials. *Chem. Rev.* **2014**, *114*, 9919–9986. [CrossRef]
17. Armaković, S.J.; Savanović, M.M.; Armaković, S. Titanium Dioxide as the Most Used Photocatalyst for Water Purification: An Overview. *Catalysts* **2022**, *13*, 26. [CrossRef]
18. Fang, W.; Xing, M.; Zhang, J. Modifications on Reduced Titanium Dioxide Photocatalysts: A Review. *J. Photochem. Photobiol. C Photochem. Rev.* **2017**, *32*, 21–39. [CrossRef]
19. Pawar, T.J.; Contreras López, D.; Olivares Romero, J.L.; Vallejo Montesinos, J. Surface Modification of Titanium Dioxide. *J. Mater. Sci.* **2023**, *58*, 6887–6930. [CrossRef]
20. Li, R.; Li, T.; Zhou, Q. Impact of Titanium Dioxide (TiO_2) Modification on Its Application to Pollution Treatment—A Review. *Catalysts* **2020**, *10*, 804. [CrossRef]

21. Pajot, N.; Papiernik, R.; Hubert-Pfalzgraf, L.G.; Vaissermann, J.; Parraud, S. Metal-Assisted Activation of the C–O Bond of 2-Hydroxyethylmethacrylate. Synthesis and Molecular Structure of $Ti_5(OPr^i)_9(\mu\text{-}OPr^i)(\mu,\eta^2\text{-}OC_2H_4O)(\mu_3,\eta^2\text{-}OC_2H_4O)_3(\mu_4,\eta^2\text{-}OC_2H_4O)$. *J. Chem. Soc. Chem. Commun.* **1995**, *17*, 1817–1819. [CrossRef]
22. Czakler, M.; Artner, C.; Schubert, U. Influence of the Phosphonate Ligand on the Structure of Phosphonate-Substituted Titanium Oxo Clusters. *Eur. J. Inorg. Chem.* **2013**, *2013*, 5790–5796. [CrossRef]
23. Czakler, M.; Artner, C.; Schubert, U. Titanium Oxo/Alkoxo Clusters with Both Phosphonate and Methacrylate Ligands. *Monatshefte Für Chem. Chem. Mon.* **2015**, *146*, 1249–1256. [CrossRef] [PubMed]
24. Mou, W.-Y.; Xie, B.; Li, X.-L.; Lai, C.; Li, T.; Chen, L.; Feng, J.-S.; Bai, X.-X.; Wu, Y.; Wu, W.-P.; et al. Tartrate-Stabilized Titanium–Oxo Clusters Containing Sulfonate Chromophore Ligands: Synthesis, Crystal Structures and Photochemical Properties. *New J. Chem.* **2021**, *45*, 10930–10939. [CrossRef]
25. Radtke, A.; Piszczek, P.; Muzioł, T.; Wojtczak, A. The Structural Conversion of Multinuclear Titanium(IV) μ-Oxo-Complexes. *Inorg. Chem.* **2014**, *53*, 10803–10810. [CrossRef] [PubMed]
26. Guo, Y.-H.; Yu, Y.-Z.; Shen, Y.-H.; Yang, L.-G.; Liu, N.-N.; Zhou, Z.-Y.; Niu, Y.-S. "Three-in-One" Structural-Building-Mode-Based Ti_{16}-Type Titanium Oxo Cluster Entirely Protected by the Ligands Benzoate and Salicylhydroxamate. *Inorg. Chem.* **2022**, *61*, 8685–8693. [CrossRef]
27. Pei, X.-Y.; He, Y.; Wang, J.-Y.; Wang, H.-Y.; Bo, Q.-B. Substituted Benzoate-Anchored Decanuclear Titanium-Oxo Clusters Featuring an Unprecedented Defective Double-Cubane Geometry. *CrystEngComm* **2023**, *25*, 1617–1625. [CrossRef]
28. Nasikhudin; Diantoro, M.; Kusumaatmaja, A.; Triyana, K. Study on Photocatalytic Properties of TiO_2 Nanoparticle in Various pH Condition. *J. Phys. Conf. Ser.* **2018**, *1011*, 012069. [CrossRef]
29. Hong, Z.-F.; Xu, S.-H.; Yan, Z.-H.; Lu, D.-F.; Kong, X.-J.; Long, L.-S.; Zheng, L.-S. A Large Titanium Oxo Cluster Featuring a Well-Defined Structural Unit of Rutile. *Cryst. Growth Des.* **2018**, *18*, 4864–4868. [CrossRef]
30. Kubiak, B.; Piszczek, P.; Radtke, A.; Muzioł, T.; Wrzeszcz, G.; Golińska, P. Photocatalytic and Antimicrobial Activity of Titanium(IV)-Oxo Clusters of Different Core Structure. *Crystals* **2023**, *13*, 998. [CrossRef]
31. Kubiak, B.; Muziol, T.M.; Jabłoński, M.; Radtke, A.; Piszczek, P. Investigation of Titanium(IV)-Oxo Complexes Stabilized with α-Hydroxy Carboxylate Ligands: Structural Analysis and DFT Studies. *Dalton Trans.* **2024**, *53*, 14457–14468. [CrossRef] [PubMed]
32. Kubiak, B.; Muzioł, T.; Wrzeszcz, G.; Radtke, A.; Golińska, P.; Jędrzejewski, T.; Wrotek, S.; Piszczek, P. Structural Characterization and Bioactivity of a Titanium(IV)-Oxo Complex Stabilized by Mandelate Ligands. *Molecules* **2024**, *29*, 1736. [CrossRef]
33. Bossmann, S.H.; Wörner, M.; Pokhrel, M.R.; Baumeister, B.; Göb, S.; Braun, A.M. Ruthenium(II)-Tris-Bipyridine/Titanium Dioxide Codoped Zeolite Y Photocatalyst: Performance Optimization Using 2,4-Xylidine (1-Amino-2,4-Dimethyl-Benzene). *Sep. Purif. Technol.* **2009**, *67*, 201–207. [CrossRef]
34. Gajardo, F.; Leiva, A.M.; Loeb, B.; Delgadillo, A.; Stromberg, J.R.; Meyer, G.J. Interfacial Electron Transfer on TiO2 Sensitized with an Axially Anchored Trans Tetradentate Ru(II) Compound. *Inorganica Chim. Acta* **2008**, *361*, 613–619. [CrossRef]
35. Ni, J.-S.; Hung, C.-Y.; Liu, K.-Y.; Chang, Y.-H.; Ho, K.-C.; Lin, K.-F. Effects of Tethering Alkyl Chains for Amphiphilic Ruthenium Complex Dyes on Their Adsorption to Titanium Oxide and Photovoltaic Properties. *J. Colloid Interface Sci.* **2012**, *386*, 359–365. [CrossRef] [PubMed]
36. Góngora, J.F.; Elizondo, P.; Hernández-Ramírez, A. Photocatalytic Degradation of Ibuprofen Using TiO2 Sensitized by Ru(II) Polyaza Complexes. *Photochem. Photobiol. Sci.* **2017**, *16*, 31–37. [CrossRef] [PubMed]
37. Sastre, F.; Bouizi, Y.; Fornés, V.; Garcia, H. Visible-Light Hydrogen Generation Using as Photocatalysts Layered Titanates Incorporating in the Intergallery Space Ruthenium Tris(Bipyridyl) and Methyl Viologen. *J. Colloid Interface Sci.* **2010**, *346*, 172–177. [CrossRef]
38. Chatterjee, D.; Edik, R.V. Prospect of Ru^{III} (Edta) in Catalysis of Bicarbonate Reduction. *CCAT* **2020**, *9*, 23–31. [CrossRef]
39. Yu, Z.; Li, Y.; Torres-Pinto, A.; LaGrow, A.P.; Diaconescu, V.M.; Simonelli, L.; Sampaio, M.J.; Bondarchuk, O.; Amorim, I.; Araujo, A.; et al. Single-Atom Ir and Ru Anchored on Graphitic Carbon Nitride for Efficient and Stable Electrocatalytic/Photocatalytic Hydrogen Evolution. *Appl. Catal. B Environ.* **2022**, *310*, 121318. [CrossRef]
40. Singha, K.; Laha, P.; Chandra, F.; Dehury, N.; Koner, A.L.; Patra, S. Long-Lived Polypyridyl Based Mononuclear Ruthenium Complexes: Synthesis, Structure, and Azo Dye Decomposition. *Inorg. Chem.* **2017**, *56*, 6489–6498. [CrossRef] [PubMed]
41. Rupp, M.; Auvray, T.; Rousset, E.; Mercier, G.M.; Marvaud, V.; Kurth, D.G.; Hanan, G.S. Photocatalytic Hydrogen Evolution Driven by a Heteroleptic Ruthenium(II) Bis(Terpyridine) Complex. *Inorg. Chem.* **2019**, *58*, 9127–9134. [CrossRef] [PubMed]
42. Li, C.-X.; Liu, Y.; Guo, Z.; Wang, Y.-J.; Guo, Z.-Y.; Lau, T.-C.; Li, W.-W. Efficient Pollutant Degradation via Non-Radical Dominated Pathway by Self-Regenerative Ru(Bpy)32+/Peroxydisulfate under Visible Light. *Chem. Eng. J.* **2020**, *400*, 125993. [CrossRef]
43. Dhanaraj, C.J.; Raj, S.S.S.; Synthesis, S.S.S.R. Structural Elucidation and Photocatalytic Studies of Some 4-Aminoantipyrine Based Ruthenium (III) Complexes. *J. Environ. Nanotechnol.* **2019**, *8*, 21–22. [CrossRef]
44. Gao, Y.; Qian, B.-F.; Wang, J.-L.; Jia, A.-Q.; Mei, Q.; Zhang, Q.-F. μ-Disulfido Complexes of Ruthenium(III) 1,1′-Dithiolate [{(Me3tacn)Ru}2(K2-S2COR)(K2-S2C = O)(μ-S2)]PF6 (Me3tacn = 1,4,7-Trimethyl-1,4,7-Triazacyclononane; R = Alkyl). *Inorganica Chim. Acta* **2023**, *548*, 121374. [CrossRef]

45. Ghosh, D.; Takeda, H.; Fabry, D.C.; Tamaki, Y.; Ishitani, O. Supramolecular Photocatalyst with a Rh(III)-Complex Catalyst Unit for CO_2 Reduction. *ACS Sustain. Chem. Eng.* **2019**, *7*, 2648–2657. [CrossRef]
46. Mongal, B.N.; Tiwari, A.; Malapaka, C.; Pal, U. Ruthenium(III)-Bis(Phenolato)Bipyridine/TiO_2 Hybrids: Unprecedented Photocatalytic Hydrogen Evolution. *Dalton Trans.* **2019**, *48*, 10070–10077. [CrossRef] [PubMed]
47. Fleming, C.N.; Dattelbaum, D.M.; Thompson, D.W.; Ershov, A.Y.; Meyer, T.J. Excited State Intervalence Transfer in a Rigid Polymeric Film. *J. Am. Chem. Soc.* **2007**, *129*, 9622–9630. [CrossRef] [PubMed]
48. Piszczek, P.; Kubiak, B.; Golińska, P.; Radtke, A. Oxo-Titanium(IV) Complex/Polymer Composites—Synthesis, Spectroscopic Characterization and Antimicrobial Activity Test. *IJMS* **2020**, *21*, 9663. [CrossRef] [PubMed]
49. Kubiak, B.; Radtke, A.; Topolski, A.; Wrzeszcz, G.; Golińska, P.; Kaszkowiak, E.; Sobota, M.; Włodarczyk, J.; Stojko, M.; Piszczek, P. The Composites of PCL and Tetranuclear Titanium(IV)-Oxo Complexes as Materials Exhibiting the Photocatalytic and the Antimicrobial Activity. *IJMS* **2021**, *22*, 7021. [CrossRef] [PubMed]
50. Aloui, F.; Jabli, M.; Hassine, B.B. Synthesis and Characterization of a New Racemic Helically Chiral Ru(II) Complex and Its Catalytic Degradation of Eriochrome Blue Black B. *Synth. Commun.* **2012**, *42*, 3620–3631. [CrossRef]
51. Motaung, T.E.; Luyt, A.S.; Bondioli, F.; Messori, M.; Saladino, M.L.; Spinella, A.; Nasillo, G.; Caponetti, E. PMMA–Titania Nanocomposites: Properties and Thermal Degradation Behaviour. *Polym. Degrad. Stab.* **2012**, *97*, 1325–1333. [CrossRef]
52. Raheem, G. Kadhim Study the Electrical and Structural Properties of (PMMA-TiO_2) Nanocomposites. *Chem. Mater. Res.* **2015**, *7*, 37–48.
53. Ravel, B.; Newville, M. *ATHENA*, *ARTEMIS*, *HEPHAESTUS*: Data Analysis for X-Ray Absorption Spectroscopy Using *IFEFFIT*. *J. Synchrotron Radiat.* **2005**, *12*, 537–541. [CrossRef] [PubMed]
54. Xu, H.; Ouyang, S.; Liu, L.; Reunchan, P.; Umezawa, N.; Ye, J. Recent Advances in TiO_2-Based Photocatalysis. *J. Mater. Chem. A* **2014**, *2*, 12642. [CrossRef]
55. Diamantis, A.A.; Dubrawski, J.V. Preparation and Structure of Ethylenediaminetetraacetate Complexes of Ruthenium(II) with Dinitrogen, Carbon Monoxide, and Other .Pi.-Acceptor Ligands. *Inorg. Chem.* **1981**, *20*, 1142–1150. [CrossRef]
56. Impert, O.; Katafias, A.; Kita, P.; Wrzeszcz, G.; Fenska, J.; Lente, G.; Fábián, I. Base Hydrolysis of Mer-Trispicolinatoruthenium(III): Kinetics and Mechanism. *Transition Met Chem* **2011**, *36*, 761–766. [CrossRef]
57. Meth-Cohn, O.; Thorpe, D.; Twitchett, H.J. Insertion Reactions of Titanium Alkoxides with Isocyanates and Carbodiimides. *J. Chem. Soc. C* **1970**, 132. [CrossRef]
58. Badea, M.; Olar, R.; Marinescu, D.; Uivarosi, V.; Nicolescu, T.O.; Iacob, D. Thermal Study of Some New Quinolone Ruthenium(III) Complexes with Potential Cytostatic Activity. *J Therm Anal Calorim* **2010**, *99*, 829–834. [CrossRef]
59. Chyba, J.; Hruzíková, A.; Knor, M.; Pikulová, P.; Marková, K.; Novotný, J.; Marek, R. Nature of NMR Shifts in Paramagnetic Octahedral Ru(III) Complexes with Axial Pyridine-Based Ligands. *Inorg. Chem.* **2023**, *62*, 3381–3394. [CrossRef]
60. Lätsch, L.; Guda, S.A.; Romankov, V.; Wartmann, C.; Neudörfl, J.-M.; Dreiser, J.; Berkessel, A.; Guda, A.A.; Copéret, C. Tracking Coordination Environment and Reaction Intermediates in Homo- and Heterogeneous Epoxidation Catalysts via Ti L2,3-Edge NEXAFS 2024. *J. Am. Chem. Soc.* **2024**, *146*, 7456. [CrossRef] [PubMed]
61. Fioretti, A.N.; Schwartz, C.P.; Vinson, J.; Nordlund, D.; Prendergast, D.; Tamboli, A.C.; Caskey, C.M.; Tuomisto, F.; Linez, F.; Christensen, S.T.; et al. Understanding and Control of Bipolar Self-Doping in Copper Nitride. *J. Appl. Phys.* **2016**, *119*, 181508. [CrossRef] [PubMed]
62. Ye, Y.; Kapilashrami, M.; Chuang, C.-H.; Liu, Y.; Glans, P.-A.; Guo, J. X-Ray Spectroscopies Studies of the 3d Transition Metal Oxides and Applications of Photocatalysis. *MRS Commun.* **2017**, *7*, 53–66. [CrossRef]
63. Wojtaszek, K.; Błachucki, W.; Tyrała, K.; Nowakowski, M.; Zając, M.; Stępień, J.; Jagodziński, P.; Banaś, D.; Stańczyk, W.; Czapla-Masztafiak, J.; et al. Determination of Crystal-Field Splitting Induced by Thermal Oxidation of Titanium. *J. Phys. Chem. A* **2021**, *125*, 50–56. [CrossRef] [PubMed]
64. Impert, O.; Pryshchepa, O.; Pomastowski, P.; Rafińska, K.; Chatterjeec, D. Redox Reaction of a RuIII(Pic)3 Complex with Cysteine: Spectral, Kinetic and Biological Studies. *Inorganica Chim. Acta* **2025**, *574*, 122401. [CrossRef]
65. Nguyen, H.L. The Chemistry of Titanium-Based Metal–Organic Frameworks. *New J. Chem.* **2017**, *41*, 14030–14043. [CrossRef]
66. Chen, X.; Peng, X.; Jiang, L.; Yuan, X.; Yu, H.; Wang, H.; Zhang, J.; Xia, Q. Recent Advances in Titanium Metal–Organic Frameworks and Their Derived Materials: Features, Fabrication, and Photocatalytic Applications. *Chem. Eng. J.* **2020**, *395*, 125080. [CrossRef]
67. Wang, J.; Cherevan, A.S.; Hannecart, C.; Naghdi, S.; Nandan, S.P.; Gupta, T.; Eder, D. Ti-Based MOFs: New Insights on the Impact of Ligand Composition and Hole Scavengers on Stability, Charge Separation and Photocatalytic Hydrogen Evolution. *Appl. Catal. B Environ.* **2021**, *283*, 119626. [CrossRef]
68. Ho, J.; Nord, M.T.; Stafford, J.P.; Stylianou, K.C. Ruthenium-Based Metal–Organic Framework Catalyst for CO_2 Fixation onto Epoxides. *Catal. Sci. Technol.* **2022**, *12*, 6998–7002. [CrossRef]

69. Liu, J.; Shi, L.; Wang, Y.; Li, M.; Zhou, C.; Zhang, L.; Yao, C.; Yuan, Y.; Fu, D.; Deng, Y.; et al. Ruthenium-Based Metal-Organic Framework with Reactive Oxygen and Nitrogen Species Scavenging Activities for Alleviating Inflammation Diseases. *Nano Today* **2022**, *47*, 101627. [CrossRef]
70. Al-Ahmed, Z.A.; Aljohani, M.M.; Sallam, S.; Alkhatib, F.M.; Alaysuy, O.; Alsharief, H.H.; Shah, R.; El-Metwaly, N.M. Synthesis of Magnetic Ruthenium Metal-Organic Frameworks for Efficient Removal of 2,4-Dichlorophenylacetic Pesticide from Aqueous Solutions: Batch Adsorption, Box-Behnken Design Optimization and Reusability. *J. Water Process Eng.* **2023**, *56*, 104444. [CrossRef]
71. Petit, C. Present and Future of MOF Research in the Field of Adsorption and Molecular Separation. *Curr. Opin. Chem. Eng.* **2018**, *20*, 132–142. [CrossRef]
72. Ghanbari, T.; Abnisa, F.; Wan Daud, W.M.A. A Review on Production of Metal Organic Frameworks (MOF) for CO_2 Adsorption. *Sci. Total Environ.* **2020**, *707*, 135090. [CrossRef] [PubMed]
73. Wang, C.; Xiong, C.; He, Y.; Yang, C.; Li, X.; Zheng, J.; Wang, S. Facile Preparation of Magnetic Zr-MOF for Adsorption of Pb(II) and Cr(VI) from Water: Adsorption Characteristics and Mechanisms. *Chem. Eng. J.* **2021**, *415*, 128923. [CrossRef]
74. Minitha, C.R.; Lalitha, M.; Jeyachandran, Y.L.; Senthilkumar, L.; RT, R.K. Adsorption Behaviour of Reduced Graphene Oxide towards Cationic and Anionic Dyes: Co-Action of Electrostatic and π–π Interactions. *Mater. Chem. Phys.* **2017**, *194*, 243–252. [CrossRef]
75. Pijović, M.; Manić, N.; Anićijević, D.V.; Krstić, A.; Mitrić, M.; Matić, T.; Janković, B. Simple and Effective One-Step Production of High-Quality Mesoporous Pyrolytic Char from Waste Tires: Rhodamine B Adsorption Kinetics and Density Functional Theory (DFT) Study. *Diam. Relat. Mater.* **2022**, *121*, 108768. [CrossRef]
76. Parcheta, M.; Świsłocka, R.; Świderski, G.; Matejczyk, M.; Lewandowski, W. Spectroscopic Characterization and Antioxidant Properties of Mandelic Acid and Its Derivatives in a Theoretical and Experimental Approach. *Materials* **2022**, *15*, 5413. [CrossRef]
77. Świsłocka, R.; Świderski, G.; Nasiłowska, J.; Sokołowska, B.; Wojtczak, A.; Lewandowski, W. Research on the Electron Structure and Antimicrobial Properties of Mandelic Acid and Its Alkali Metal Salts. *IJMS* **2023**, *24*, 3078. [CrossRef] [PubMed]
78. García-Rubiño, M.E.; Matilla-Hernández, A.; Frontera, A.; Lezama, L.; Niclós-Gutiérrez, J.; Choquesillo-Lazarte, D. Dicopper(II)-EDTA Chelate as a Bicephalic Receptor Model for a Synthetic Adenine Nucleoside. *Pharmaceuticals* **2021**, *14*, 426. [CrossRef]
79. Barbas, R.; Font-Bardia, M.; Frontera, A.; Prohens, R. Polymorphism in the 1/1 Pterostilbene/Picolinic Acid Cocrystal. *Cryst. Growth Des.* **2022**, *22*, 590–597. [CrossRef] [PubMed]
80. Liu, C.; Hu, J.; Liu, W.; Zhu, F.; Wang, G.; Tung, C.; Wang, Y. Binding Modes of Salicylic Acids to Titanium Oxide Molecular Surfaces. *Chem. A Eur. J.* **2020**, *26*, 2666–2674. [CrossRef] [PubMed]
81. Yu, Y.-Z.; Zhang, Y.-R.; Geng, C.-H.; Sun, L.; Guo, Y.; Feng, Y.-R.; Wang, Y.-X.; Zhang, X.-M. Precise and Wide-Ranged Band-Gap Tuning of Ti_6 -Core-Based Titanium Oxo Clusters by the Type and Number of Chromophore Ligands. *Inorg. Chem.* **2019**, *58*, 16785–16791. [CrossRef] [PubMed]
82. Kinnunen, T.-J.J.; Haukka, M.; Pakkanen, T.A. Alkoxycarbonyl Substituted Ruthenium Mono(Bipyridine) Complexes: Steric Effects of the Bipyridine Substituents. *J. Organomet. Chem.* **2002**, *654*, 8–15. [CrossRef]
83. Kinnunen, T.-J.J.; Haukka, M.; Pesonen, E.; Pakkanen, T.A. Ruthenium Complexes with 2,2′-, 2,4′- and 4,4′-Bipyridine Ligands: The Role of Bipyridine Coordination Modes and Halide Ligands. *J. Organomet. Chem.* **2002**, *655*, 31–38. [CrossRef]
84. Cruz-Ortiz, B.R.; Hamilton, J.W.J.; Pablos, C.; Díaz-Jiménez, L.; Cortés-Hernández, D.A.; Sharma, P.K.; Castro-Alférez, M.; Fernández-Ibañez, P.; Dunlop, P.S.M.; Byrne, J.A. Mechanism of Photocatalytic Disinfection Using Titania-Graphene Composites under UV and Visible Irradiation. *Chem. Eng. J.* **2017**, *316*, 179–186. [CrossRef]
85. Webb, M.I.; Walsby, C.J. EPR as a Probe of the Intracellular Speciation of Ruthenium(Iii) Anticancer Compounds. *Metallomics* **2013**, *5*, 1624. [CrossRef] [PubMed]
86. *ISO 10678:2010*; Fine Ceramics (Advanced Ceramics, Advanced Technical Ceramics)—Determination of Photocatalytic Activity of Surfaces in an Aqueous Medium by Degradation of Methylene Blue 2010. ISO: Geneva, Switzerland, 2010.
87. Ali, M.A.; Maafa, I.M.; Qudsieh, I.Y. Photodegradation of Methylene Blue Using a UV/H_2O_2 Irradiation System. *Water* **2024**, *16*, 453. [CrossRef]
88. Mouele, E.S.M.; Tijani, J.O.; Masikini, M.; Fatoba, O.O.; Eze, C.P.; Onwordi, C.T.; Myint, M.T.Z.; Kyaw, H.H.; Al-Sabahi, J.; Al-Abri, M.; et al. Spectroscopic Measurements of Dissolved O3, H2O2 and OH Radicals in Double Cylindrical Dielectric Barrier Discharge Technology: Treatment of Methylene Blue Dye Simulated Wastewater. *Plasma* **2020**, *3*, 59–91. [CrossRef]
89. Zuo, R.; Du, G.; Zhang, W.; Liu, L.; Liu, Y.; Mei, L.; Li, Z. Photocatalytic Degradation of Methylene Blue Using TiO_2 Impregnated Diatomite. *Adv. Mater. Sci. Eng.* **2014**, *2014*, 1–7. [CrossRef]
90. Ehlert, M.; Radtke, A.; Topolski, A.; Śmigiel, J.; Piszczek, P. The Photocatalytic Activity of Titania Coatings Produced by Electrochemical and Chemical Oxidation of Ti6Al4V Substrate, Estimated According to ISO 10678:2010. *Materials* **2020**, *13*, 2649. [CrossRef] [PubMed]
91. Sifat, M.; Shin, E.; Schevon, A.; Ramos, H.; Pophali, A.; Jung, H.-J.; Halada, G.; Meng, Y.; Olynik, N.; Sprouster, D.J.; et al. Photocatalytic Degradation of Crystal Violet (CV) Dye over Metal Oxide (MOx) Catalysts. *Catalysts* **2024**, *14*, 377. [CrossRef]

92. Sanakousar, M.F.; Vidyasagar, C.C.; Jiménez-Pérez, V.M.; Jayanna, B.K.; Mounesh; Shridhar, A.H.; Prakash, K. Efficient Photocatalytic Degradation of Crystal Violet Dye and Electrochemical Performance of Modified MWCNTs/Cd-ZnO Nanoparticles with Quantum Chemical Calculations. *J. Hazard. Mater. Adv.* **2021**, *2*, 100004. [CrossRef]
93. Hunge, Y.M.; Uchida, A.; Tominaga, Y.; Fujii, Y.; Yadav, A.A.; Kang, S.-W.; Suzuki, N.; Shitanda, I.; Kondo, T.; Itagaki, M.; et al. Visible Light-Assisted Photocatalysis Using Spherical-Shaped $BiVO_4$ Photocatalyst. *Catalysts* **2021**, *11*, 460. [CrossRef]
94. Som, I.; Roy, M.; Saha, R. Advances in Nanomaterial-based Water Treatment Approaches for Photocatalytic Degradation of Water Pollutants. *ChemCatChem* **2020**, *12*, 3409–3433. [CrossRef]
95. Štrbac, D.; Aggelopoulos, C.A.; Štrbac, G.; Dimitropoulos, M.; Novaković, M.; Ivetić, T.; Yannopoulos, S.N. Photocatalytic Degradation of Naproxen and Methylene Blue: Comparison between ZnO, TiO_2 and Their Mixture. *Process Saf. Environ. Prot.* **2018**, *113*, 174–183. [CrossRef]
96. AlHamedi, F.H.; Rauf, M.A.; Ashraf, S.S. Degradation Studies of Rhodamine B in the Presence of UV/H_2O_2. *Desalination* **2009**, *239*, 159–166. [CrossRef]
97. Zuorro, A.; Lavecchia, R. Evaluation of UV/H_2O_2 Advanced Oxidation Process (AOP) for the Degradation of Diazo Dye Reactive Green 19 in Aqueous Solution. *Desalination Water Treat.* **2014**, *52*, 1571–1577. [CrossRef]
98. Suriye, K.; Lobo-Lapidus, R.J.; Yeagle, G.J.; Praserthdam, P.; Britt, R.D.; Gates, B.C. Probing Defect Sites on TiO_2 with [$Re_3(CO)_{12}H_3$]: Spectroscopic Characterization of the Surface Species. *Chem. Eur. J.* **2008**, *14*, 1402–1414. [CrossRef] [PubMed]
99. Canevali, C.; Chiodini, N.; Morazzoni, F.; Scotti, R. Electron Paramagnetic Resonance Characterization of Ruthenium-Dispersed Tin Oxide Obtained by Sol–Gel and Impregnation Methods. *J. Mater. Chem.* **2000**, *10*, 773–778. [CrossRef]